Technische Universität Ilmenau
Fakultät für Mathematik und
Naturwissenschaften
Institut für Physik

Topological phase transitions of HgSe under uniaxial pressure

A thesis submitted for the degree of
Master of Science

Lars Winterfeld

Supervising Professor:
Prof. Dr. Erich Runge

Second Reviewer:
Prof. Dr. Martina Hentschel

Ilmenau, February 26, 2013

urn:nbn:de:gbv:ilm1-2013200217

Acknowledgement

I would like to thank everybody who supported me while writing this thesis.

Special thanks go to my supervisor during my stay in the USA, Dr. Nicholas Kioussis, who was always a source of encouragement. From the people in his group, I want to thank especially Dr. Jin Li for an introduction into the Vasp software and several fruitful discussions. This work would not have been possible without Dr. Luis Agapito, who contributed an implementation to calculate the $\mathbb{Z}_2$ invariant. Son Giang helped a lot to fix technical problems on the compute cluster.

As always, Prof. Dr. Erich Runge has been motivating and inspiring. I want to thank him for several physical discussions.

M.Sc. Stefan Brechtken and Dipl.-Math. Leslie Leben deserve credit for proof-reading large parts of this text.

Erklärung: Hiermit versichere ich, dass ich diese Masterarbeit selbständig verfasst und nur die angegebenen Quellen und Hilfsmittel verwendet habe. Alle von mir aus anderen Veröffentlichungen übernommenen Passagen sind als solche gekennzeichnet.
Alle Darstellung sind selbst erstellt.

Ilmenau, February 26, 2013 .....

Lars Winterfeld

Abstract in English:

Using ab initio calculations, the influence of uniaxial pressure on the band structure of the zinc-blende semi-metal mercury selenide (HgSe) is investigated. Both small tensile and compressive strain along both the [001] and [110] directions open up a band gap in the vicinity of Γ point of up to 37 meV. Calculations of the $\mathbb{Z}_2$ invariant show that HgSe is in the phase of a topological insulator under uniaxial compression of about -5%. Both stronger compression and expansion cause a transition into the phase of a normal insulator. Calculations of a HgSe slab system show surface states with great similarity to Dirac cones of known topological insulators.

The work is arranged into an introduction, which provides an overview; a chapter to present the theoretical basics; a chapter for the results and a final section for conclusions.

The thesis is written in English.

Zusammenfassung in Deutsch:

Mittels ab initio Rechnungen wird der Einfluss von uniaxialem Druck auf die Bandstruktur des Zinkblende-Halbmetalls Quecksilberselenid (HgSe) untersucht. Sowohl geringfügige Dehnung als auch Kompression entlang der [001] und [110] Richtungen öffnen eine Bandlücke in der Nähe des Γ-Punktes von bis zu 37 meV. Berechnungen der $\mathbb{Z}_2$-Invariante zeigen, dass sich HgSe unter uniaxialer Kompression von etwa -5% in der Phase eines Topologischen Isolators befindet. Sowohl stärkere Kompression als auch Dehnung verursachen einen Übergang in die Phase eines gewöhnlichen Isolators. Rechnungen an einem HgSe-Mehrschichtsystem zeigen Oberflächenzustände mit großer Ähnlichkeit zu Dirac-Kegeln bekannter Topologischer Isolatoren.

Die Arbeit gliedert sich eine überblick-bietende Einleitung, eine Kapitel zum Darstellen theoretischer Grundlagen, einen Ergebnisteil sowie ein Abschlusskapitel für Schlussfolgerungen.

Die Arbeit ist in englischer Sprache verfasst.

Lists and Definitions

List of symbols

The following symbols are used throughout this thesis. Symbols not listed below have multiple meanings, which are always defined in the text.

Symbol	**Meaning**
$\propto$	proportional to
$\cong$	isomorphic
$\approx$	approximately the same
$\bar{c}$	the complex conjugate of c
$\vec{\nabla}$	"nabla" operator, $\nabla_i := \frac{\partial}{\partial x_i}$
Θ	time-reversal operator
$\mathbb{C}$	the set of complex numbers
$\mathbb{N}$	the set of natural numbers, including 0
$\mathbb{N}_+$	the set of positive natural numbers
$\mathbb{R}$	the set of real numbers
$\mathbb{R}_{\geq 0}$	the non-negative real numbers
$\mathbb{Q}$	the set of rational numbers
$\mathbb{Z}$	the set of integer numbers
$\mathbb{Z}_2$	$\mathbb{Z}_2 \cong \{0, 1\}$ with addition mod 2
$\mathbb{I}_n$	identity matrix in n dimensions
Pf	Pfaffian of a anti-symmetric matrix
Γ	the point in the Brillouin zone where $\vec{k} = \vec{0}$
Γ_n, Δ_n, Σ_n	a band of the nth irreducible representation at the Γ point, along the Δ or Σ line in the Brillouin zone, respectively
Δ^Γ	direct energy gap at the Γ-point
δ_a	$\delta_a \in \{-1, +1\}$ at a TRIM point $\vec{k_a}$
ε	strain value, $\varepsilon \in \mathbb{R}$
$\overleftrightarrow{\varepsilon}$	strain tensor, $\overleftrightarrow{\varepsilon} \in \mathbb{R}^{3\times 3}$
ε_0	vacuum permittivity
η	$\eta := \sigma_H \cdot \frac{h}{e^2}$

Symbol	**Meaning**
ν, ν_0, ν_2, ν_2, ν_3	topological invariant
ρ	electron density
σ_H	Hall conductivity, corresponds to σ_{xy} in the σ-tensor
τ	kinetic energy density
Ψ	wave function
ω	angular frequency
a	lattice constant
$\vec{a_1}$, $\vec{a_2}$, $\vec{a_3}$	primitive lattice vectors
$\vec{A}$	Berry connection
$\vec{B}$	magnetic field
B_0	bulk modulus
B_0'	derivative of bulk modulus
c_{ij}	elastic constant
c_{MBJ}	c parameter for MBJ functional
e	elementary charge
E	energy
E_F	Fermi energy
E_{gap}	fundamental energy gap
E_{VBM}	energy of the valence band maximum
$\vec{\mathcal{F}}$	Berry curvature
h	Planck's constant (elementary action)
$\hbar$	$\hbar := \frac{h}{2\pi}$
$\mathcal{H}$	Hamilton operator
$\mathcal{H}_{SO}$	Hamilton operator of spin orbit interaction
I	electric current
$\vec{k} = (k_x, k_y, k_z)^T$	wave vector (in reciprocal space)
$\vec{k_a}$	$\vec{k}$-vector of a TRIM point
$\vec{k}_D$	Dirac point in $\vec{k}$-space
k_B	Boltzmann's constant
nlm	atomic quantum numbers
$\vec{L}$	angular momentum operator

Symbol	**Meaning**
m	electron mass
N	number of electrons
$\mathcal{P}$	parity (symmetry under space inversion)
P	polarization
$\vec{r}$, $\vec{R}$	positions in real space
$\vec{S} = (S_x, S_y, S_z)$	spin vector
$\mathcal{T}$	time-reversal (symmetry)
u	Bloch function
U(1)	circle group with $U(1) := \{c \in \mathbb{C} \mid \lvert c\rvert = 1\}$
U_H	Hall voltage
$\mathcal{V}$	volume
V_0	equilibrium volume
V	potential
v_F	Fermi velocity
x, y	position components
z, z_0, z_π	topological invariant for a 2D plane
Z_i	atomic number (proton number)

List of abbreviations

Abbreviation	**Meaning**
2D	two-dimensional
3D	three-dimensional
CBM	conduction band minimum
DFT	Density Functional Theory
Fig.	Figure
FQHE	Fractional Quantum Hall Effect
GGA	Generalized Gradient Approximation
g.s.	ground state
GW	ab-initio method based on Greens function (G)
	and Coulomb screening (W)
HgSe	mercury selenide
IQHE	Integer Quantum Hall Effect
LDA	Local Density Approximation
MBJLDA	LDA-based meta-functional with Modified Becker Johnsen potential
PBE	PBE functional
QSHI	Quantum Spin Hall Insulator
TRIM	Time-Reversal-Invariant Momenta
VBM	valence band maximum

Contents

1 Introduction **13**

1.1 The Phenomenon 13

1.2 Historical Overview 13

1.2.1 Classical Hall and Integer Quantum Hall Effect 14

1.2.2 Fractional Quantum Hall Effect 16

1.2.3 Graphene 17

1.2.4 2D Topological Insulators 17

1.2.5 3D Topological Insulators 20

1.2.6 Experimental Findings 21

1.2.7 Methods of Prediction and Objective of this Thesis . . . 21

1.3 Possible Applications And New Physics 23

1.3.1 Spintronics 23

1.3.2 Topological Superconductors 24

1.3.3 Majorana Fermions and Quantum Computation 25

1.3.4 Axion Electrodynamics and The Topological Magnetoelectric Effect 25

2 Theory **26**

2.1 Density Functional Theory (DFT) 26

2.1.1 Hohenberg Kohn Theorem 27

2.1.2 Self-Consistent Loop 28

2.1.3 Functionals 29

2.2 Selected Aspects of Quantum and Solid State Physics 31

2.2.1 The Concept of Band Structures 31

2.2.2 Time Reversal and Kramer's Theorem 32

2.2.3 Strain Tensor and Elastic Constants 33

2.2.4 Character Tables 33

2.3 Topological Insulators 35

2.3.1 TKNN Argument 35

2.3.2 Topological Z2 Classification 36

2.3.3 Computing the Z2 Invariant 42
2.3.4 Band Inversion and Gap Closing 44
2.3.5 Surface States 45

3 Results for HgSe **46**
3.1 Electronic Structure of HgSe in Equilibrium 46
3.1.1 States at the Γ-Point 47
3.1.2 Results of Previous Research 47
3.1.3 Basis for further Investigations 48
3.2 Electronic Structure of HgSe Under Strain 50
3.2.1 Hydrostatic Pressure 52
3.2.2 Uniaxial Strain along [001] 53
3.2.3 Uniaxial Strain Along [110] 55
3.2.4 Evolution of the Energy Levels Under Strain 57
3.3 Topological Phase Transitions 58
3.3.1 Change of the Topological Invariant For Different Strains 58
3.3.2 Possible Explanation for the Topological Phase Transitions 60
3.4 Surface States 62

4 Conclusions **65**
4.1 Summary 65
4.2 Critique 66
4.3 Outlook 68

5 Appendix **69**
5.1 DFT Parameters 69
5.2 MBJLDA 70
5.3 Properties Odd and Even under $\mathcal{P}$ and $\mathcal{T}$ 71

Chapter 1

Introduction

This chapter introduces Topological Insulators phenomenologically and provide a short historical overview of their theoretical and experimental discovery. Afterwards, the relevance of research in this area is stressed by mentioning some possible future applications.

1.1 The Phenomenon

Phenomenologically, a Topological Insulator (TI) is a solid out of a single material in a phase of matter which allows spin-polarized conduction within a few atomic layers of the surface, while it is insulating in the spatially inner region. Spin-polarized conduction means that electrons with opposite wave vectors have opposite spins [1]. Back-scattering of electrons would therefore require a spin-flip, which is strongly suppressed in the absence of magnetic impurities [2]. TIs are therefore expected to show very high conductance that remains robust against moderate disorder, (non-magnetic) impurities and possibly other forms of lattice defects.

1.2 Historical Overview

Topological Insulators were predicted theoretically for the first time in 2005 [3–6] and experimentally confirmed shortly afterwards [7–11]. Several lines of development in physics were "knotted" together to form this new research field, most noticeably works on graphene [12, 13], the quantum Hall effect [14] and its understanding in the words of mathematical topology [15, 16]. Therefore, the next sections briefly reviews those discoveries; while the chapter thereafter introduces the theory behind Topological Insulators in a more stringent, but non-chronological way.

1.2.1 Classical Hall and Integer Quantum Hall Effect

In 1879, Edwin Hall discovered [17] that a thin (semi-)conducting plate carrying an electric current I induces a voltage difference U_H transverse to the direction of the current when it is placed in a magnetic field B. In addition to I and B, the value of U_H depends on the thickness d of the plate (parallel to B) and a material-specific constant A_H:

$$U_H = A_H \, \frac{I \, B}{d} \, . \tag{1.1}$$

Consequently, the classical Hall conductivity $\sigma_H := \frac{I}{U_H} = \frac{d}{A_H \, B}$ is indirectly proportional to B - allowing a Hall probe to easily measure B.

However, for strong magnetic fields at low temperatures, quantum effects start to be important. In 1980, Klaus von Klitzing[1] experimentally found that in this case the conductivity σ_H is *quantized* [14], i.e., it only takes integer multiples $\eta \in \mathbb{Z}$ of a fundamental constant:

$$\sigma_H = \eta \, \frac{e^2}{h}, \tag{1.2}$$

where e is the elementary charge and h is Planck's constant.

This effect can be explained theoretically by modeling the plate as a one-electron quantum system, in which the B-field causes quantized energy levels $E_n = \hbar\omega_c(n + \frac{1}{2})$, known as *Landau levels*, with the cyclotron frequency $\omega_c = \frac{e\,B}{m}$, where m is the electron mass. At low temperatures, only the states below the Fermi energy E_F are occupied (in a good approximation). Thus, for each given B, an integer number of Landau levels is occupied and the energy difference between two levels $\Delta E = \hbar\frac{e\,B}{m}$ is large for large B. This ultimately results in the quantized conductivity, which is spatially confined to the boundary of the Hall plate [18].

In 1982, another argument to understand the quantized Hall conductivity was introduced by Thouless, Kohmoto, Nightingale and Nijs (TKNN) [15]. Interestingly, the Hall conductivity σ_H of the entire system is calculated as an integral over the Bloch wave functions in the first Brillouin zone. For topological reasons more detailedly explained in section 2.3.1, this integral evaluates only to multiples of an integer (η).

[1] Nobel prize 1985

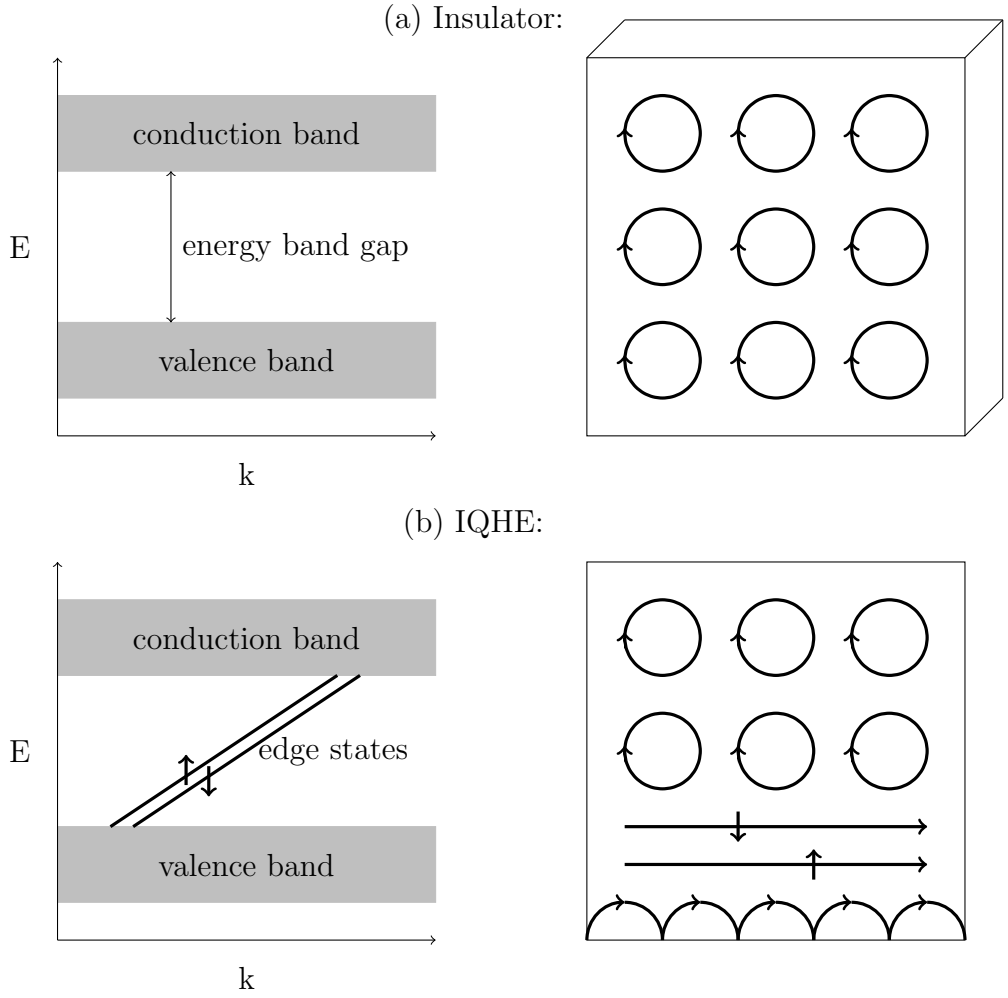

Figure 1.1: (a) The sketch of an insulator (right): all electrons are localized on a specific atom. Conduction (thought of as hopping of electrons) requires a finite energy, therefore the band scheme (left) has a gap. (b) IQHE in the presence of a magnetic field $\vec{B}$. In a 2D plate sketched on the right, the circular motion of electrons is interrupted by the boundary, leading to "skipping orbits" and conduction along the edge along one direction only for both up ($\uparrow$) and down ($\downarrow$) spin electrons. The corresponding band structure on the left has a gap in the bulk, but conducting edge states (shown for one edge only). Bands for up and down spins are not drawn on top of each other only for illustrative reasons. Figure follows the idea of [19].

1.2.2 Fractional Quantum Hall Effect

In 1982, Gossard, Störmer and Tsui[2] discovered [20] that the above η (eq. 1.2) can also take fractional values like $\frac{1}{3}$, $\frac{2}{5}$, $\frac{2}{3}$, $\frac{3}{5}$ or $\frac{5}{2}$, $\eta \in \mathbb{Q}$. Consequently, this effect was termed Fractional Quantum Hall Effect (FQHE), while Klitzing's discovery is now referred to as Integer Quantum Hall Effect (IQHE) [18]. The FQHE occurs in strongly correlated systems and is therefore inherently a many-body effect. Strong correlation implies that one electron cannot change its state independently from other electrons. Therefore, the movement of electrons can be thought of as complicated "dancing patterns", resulting in situations in which the system is better to describe by the movement of those patterns (rather than the movement of fundamental particles). This can be described by quasi-particles - in case of the FQHE by *composite fermions* carrying fractional charge.

Besides the fractional charge, the FQHE carries another significant novelty descending upon theoretical physics: Landau's theory of phases and their transitions based on symmetries and their breaking is not sufficient to understand this new and novel phase of matter. Different fractional charges in the FQHE are not associated with the breaking of any symmetry in Landau's sense [21,22]. In hope for a better overall understanding, physicists therefore considered a new framework of classification beyond classical symmetries, namely *topological order*, introduced by Wen [23]. It is built upon correlations in the complex-valued many-body ground-state wavefunction $\Psi(\vec{r_1}, \ldots, \vec{r_N})$, whereas classical symmetry classifications only consider the correlation function within the positive-valued many-particle probability distribution $|\Psi|^2(\vec{r_1}, \ldots, \vec{r_N})$.[3] Consequently, topological order has more information (esp. the phase factor) and allows for a more diverse characterization, which should contain classical orders (phases) in some limit.

[2]Nobel prize for Laughlin, Störmer and Tsui in 1998

[3]In that sense, Wen considers superconductivity to contain non-trivial topological order [21] and stresses that it cannot be characterized by breaking symmetries [22].

1.2.3 Graphene

Graphene is a modification of carbon in a planar[4] honeycomb lattice. Besides its discrete 2D lattice symmetry, graphene is also invariant under time-reversal ($\mathcal{T}$) and inversion ($\mathcal{P}$). Due to the combination of these symmetries, the conduction and valence band touch each other at two isolated points $\vec{k_D}$ and $-\vec{k_D}$ with linear dispersion. Since the resulting band structure is very well described by the two-dimensional massless Dirac-Hamiltonian, the shape of the electronic structure is called a Dirac cone and $\pm\vec{k_D}$ are Dirac points. All time-reversal ($\mathcal{T}$) invariant systems necessarily have an even number of Dirac points, due to the fermion doubling theorem [24][5]. Breaking $\mathcal{T}$ (or $\mathcal{P}$) will introduce a gap into the band structure; this can be done, e.g., using an magnetic field (or mechanical deformation). In this case, graphene may either preserve zero Hall conductance $\sigma_H = 0$ or transition into the IQHE state ($\eta \in \mathbb{N}$). Using the calculation of the Berry flux [26], these phases can again be identified using an integral over the 2D Brillouin zone.

1.2.4 2D Topological Insulators

In 2005, Kane and Mele studied a graphene-inspired tight minding model of $\mathcal{T}$-invariant 2D systems, which have a band gap [3, 4]. For certain parameters, there are edge states that crossing the Fermi energy, leading to a new phase of matter. Although the TKNN-invariant is necessarily $\eta = 0$ in this case, there is a new $\mathbb{Z}_2$ invariant $\nu \in \{0, 1\}$, which can again be computed from the Bloch functions in the Brillouin zone. While $\nu = 0$ marks the phase of a trivial insulator, $\nu = 1$ corresponds to the novel phase of a Quantum Spin Hall Insulator (QSHI), also known as 2D Topological Insulator (2DTIs) [1]. The QSHI phase always has metallic edges states, which allow one-dimensional charge transport and are chircal, i.e. transport in one direction is allowed for one spin orientation only. Topologically, semiconductors are also insulators, because they have an energy gap.

[4] Graphene planes can be macroscopically large, while the "height" is on atomic scale.

[5] The original reference [24] only discusses a translational invariant lattice with a real and local action of a free fermion. Still, the "fermion doubling problem" applies more generally [25].

If the spin component perpendicular to the plane S_z is conserved, then each spin direction has its own TKNN-invariant ($\eta_\uparrow$ and $\eta_\downarrow$). In the simplest case, the corresponding Hamilton operator will then decouple into two copies of a simpler Hamiltonian, for the two opposite spin directions. Applying an electric field will then cause $\uparrow$ and $\downarrow$ spins to have Hall currents flowing in opposite directions. This is compatible with $\mathcal{T}$-symmetry, which flips both spin and the sign of the conductivity. Thus, the total Hall conductance σ_H is zero ($\eta_\uparrow + \eta_\downarrow = 0$), but there is a *spin Hall conductivity*, which is non-zero in general, $\eta_\uparrow - \eta_\downarrow \neq 0$. This difference needs to caused by an effect separating the two spin directions in energy. Kane and Mele had the idea that this is possible without a magnetic field (thus, conserving $\mathcal{T}$-symmetry), using the intrinsic the spin-orbit interaction [3]. They argue that although disorder, interaction, $\mathcal{P}$-breaking etc. will destroy the quantization of the spin Hall conductivity, the topological ν-phase will be robust as long as $\mathcal{T}$-symmetry is preserved.

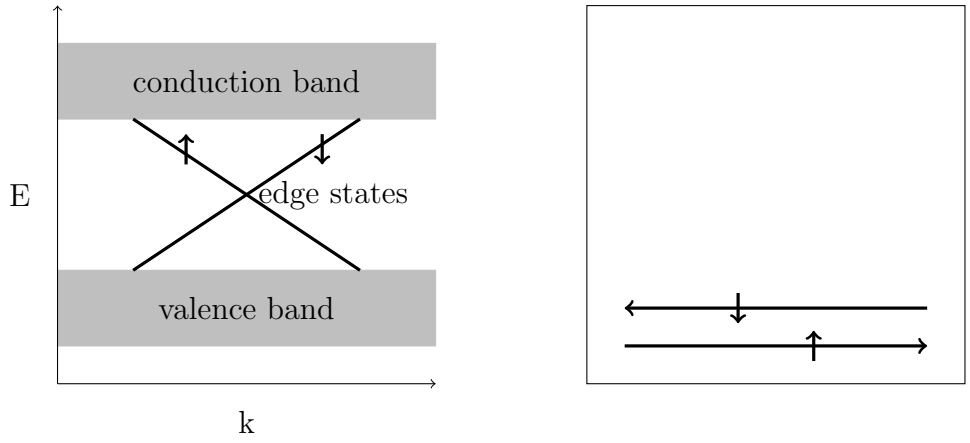

Figure 1.2: Sketch of a QHSE plate, also known as 2D TI. Just like the IQHE, there is conductance only on the boundary (symbolized by the long arrows on the right, which are not drawn on top of each other only for illustrative reasons). However, opposite spins ($\uparrow, \downarrow$) propagate into opposite directions (at the same time and space). The corresponding band structure is sketched on the left, making it obvious that the only available state for back-scattering has opposite spin. Time reversal would flip both spin and $\vec{k}$ direction, such that this state is time-reversal invariant (contrary to the IQHE, where the $\vec{B}$ explicitly breaks the $\mathcal{T}$-symmetry). Figure follows the idea of [19].

Therefore, the construction of the new invariant ν is based on a careful examination of the role of the time-reversal operator Θ, which has the property that $\Theta^2 = -1$ for spin-$\frac{1}{2}$-particles (like electrons)[6]. Fu and Kane proposed [27] to compute the invariant ν in the following way: Choose the Bloch functions $u_n(\vec{k}, \vec{r})$ continuous through the Brillouin zone and construct a quadratic unitary matrix $w_{mn}(\vec{k}) := \langle u_m(\vec{k})|\Theta|u_n(-\vec{k})\rangle$. It is antisymmetric on four special $\vec{k_a}$-points in the 2D Brillouin zone. These point are called Time Reversal Invariant Momenta (TRIM), for reasons explained in later in section 2.2.2. Using the Pfaffian, four numbers $\delta_a \in \{-1, +1\}$ are calculated: $\delta_a := \mathrm{Pf}[W(\vec{k_a})]/\sqrt{\mathrm{Det}[W(\vec{k_a})]}$. The invariant $\nu \in \mathbb{Z}_2$ is then chosen such that $(-1)^\nu = \delta_1 \cdot \delta_2 \cdot \delta_3 \cdot \delta_4$.

Originally, Kane and Mele speculated that the non-trivial $\nu = 1$ phase might exist in graphene. While it turned out later that the spin-orbit coupling is too weak in graphene, other materials are indeed in the QSHI phase.

It should be noted that the topological phases marked by ν are not to be confused with the entirely different concept of "topological order", mentioned above in the context of the FQHE. It appears that so far no unified theory has been established which is able to simultaneously explain the existence of all of the above phases, i.e. IQHE ($\eta \in \mathbb{Z}$), FQHE (different $\eta \in \mathbb{Q}$) and QSHI ($\eta = 0$, $\nu \in \mathbb{Z}_2$).

[6]Time-reversal is commonly referred to by two symbols: $\mathcal{T}$ (in context of the symmetry) and Θ (as the corresponding operator).

1.2.5 3D Topological Insulators

In three dimensions, there are eight TRIM points and four different topological indices $(\nu_0; \nu_1, \nu_2, \nu_3)$. Analogously to the 2D case, ν_0 is calculated as a product of eight δ_i in three dimensions. If $\nu_0 = 1$, then the material in question will be a "strong" topological insulator, which always has an odd number of Dirac cones on each surface [5]. If $\nu_0 = 0$, the system is either a trivial insulator or a "weak" TI. Weak TIs can be produced, e.g., by stacking multiple layer of a 2D TI. In this case, the surface states are generally anisotropic and are unfortunately easily localized by disorder. The indices ν_1, ν_2 and ν_3 classify the weak TIs further (see [5]). However, only strong TI materials ($\nu_0 = 1$) are of interest in this thesis.

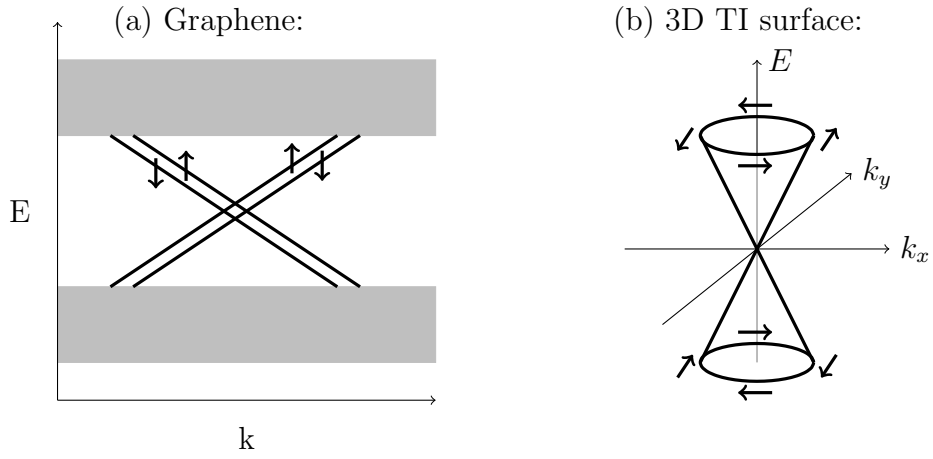

Figure 1.3: (a) The electronic structure of graphene has Dirac cones, but each state is spin degenerate. Therefore, backscattering is not suppressed. (b) Surface of a 3D TI: a single non-degenerate Dirac cone (in general, a 3D TI has an odd number of Dirac cones on the surface). It is worth mentioning that the Fermi energy has no particular reason to coincide with the Dirac point.

1.2.6 Experimental Findings

Several materials are predicted to be 3D TIs. Some of them are already confirmed by experiment. Experiments usually probe the surface band structure using Angle-Resolved Photo-Emission Spectroscopy (ARPES) to test whether it possesses a Dirac cone. An $Bi_{1-x}Sb_x$ alloy became the first known 3D TI material, found by ARPES experiments in 2008 [9]. Spin-resolved APRES proved that the surface states are indeed singly degenerate and that their spin is strongly dependent on the electron momentum $\vec{k}$ (spin-chirality) [28, 29]. Fourier-transform Scanning Tunneling Spectroscopy (FT-STS) can further be used to test the absence of back-scattering on impurities. Measurements suggest the stability of the Dirac states also at room temperature [9].

Possible TI materials include pure elements, (strained) binary compounds, alloys, quantum-wells, ternary half-Heusler compounds, (thallium-based) chalcopyrites and quaternary compounds. Generally, at least one heavy element is apparently involved in each of the TI materials. Table 1.1 provides a list of selected TI materials. An extended list can be found in [30].

1.2.7 Methods of Prediction and Objective of this Thesis

In order to predict computationally whether a material will be a TI, the following methods are commonly employed.

- *Surface states*: Several layers (usually ≥ 10) are stacked on top of each other to form a slab, for which the electronic structure is calculated. A material is then considered a TI if a Dirac cone is found in the surface states, which are extracted from the results of the calculation. Due to the large number of required atoms, these computations are very demanding with respect to both time and memory.

- *Adiabatic continuity*: If the band structure of a material can be deformed into one from a known TI material along a parameter path that keeps the gap open at all times, the material in question will also be a TI, because both materials are in the same topological equivalence class.

Compound	Theory	Experiment
Sb (antimony)	[5]	[28, 29]
$\alpha - Sn$ (grey tin)	[5]	-
strained $HgTe$	[5]	[31]
strained $InSb$	[32]	-
$Bi_{1-x}Sb_x$	[5]	[9, 28, 33]
Bi_2Se_3	[11, 34]	[10]
Bi_2Te_3	[11, 34]	[35, 36]
Sb_2Te_3	[11, 34]	[36]
$HgTe/CdTe$ quantum well	[7]	[8]
$PtLuSb$	[37–41]	[42]
$ScAuPb$	[37–41]	-
$YPtBi$	[37–41]	[43]
$AuTlSe_2$	[44]	-
$HgSnSb_2$	[44]	-
$CuTlTe_2$	[44]	-
$Ag_2HgPbSe_4$	[45]	-
$Cu_2ZnGeSe_4$	[46]	-

Table 1.1: List of selected 3D TI materials, grouped into the following groups: pure elements, (strained) binary compounds, alloys, quantum-wells, ternary half-Heusler compounds, (thallium-based) chalco-pyrites and quaternary compounds. The theory column cites predictions and the Experiment column refers to experimental confirmations.

- *Band inversion*: Bands can be viewed as combination of atomic orbitals. Normally, conduction bands are mostly combinations of s-orbitals, while valance bands come from p-orbitals. However, in known TI materials like HgTe, the ordering is the other way around. Further, in the model of Kane and Mele, spin-orbit coupling exchanges the ordering of conduction and valence band. Thus, band inversion (at the TRIM points) of s and p states is another often-used criterion.

- *Topological invariant*: The most reliable method to determine the topological phase is the calculation of the topological invariant ν_0. Possible implementations will be discussed in section 2.3.3.

On basis of the TI-theory summarized in the next chapter, a main result of this thesis is presented in chapter 3, namely enlarging the list of 3D TI materials. Using numerical calculations, HgSe is predicted to become a 3D TI under uniaxial strain.

1.3 Possible Applications And New Physics

TIs provoke a myriad of ideas for new physics[7] and possible applications, out of which only four should be mentioned here.

1.3.1 Spintronics

Current microelectronics relies on charge transport to process information. Spintronics (a portmanteau of "spin transport electronics") is based on the idea of using the spin of electrons instead of (or, additional to) the charge, hoping for "cold" information processing, i.e. with reduced (or no) dissipation. In order to create such "spin logic circuits" [47], one can either operate a device in a cycle which "pumps" spin [48], or, use materials which intrinsically separate the spin directions spatially. Due to the Dirac cone on the surface, TIs are well-suited for this purpose. When TIs are studied in slab geometry, the surface-states are not spin-degenerate (as in graphene), but each Dirac cone has an entangled partner on the opposite surface.

[7] which go partly far beyond the author's comprehension

Applying a (perpendicular) magnetic field to the TI replaces the Dirac cone by the Landau levels of the IQHE. Interestingly, however, the lowest level has zero energy and thus exhibits particle-hole symmetry, such that the sign of the Hall conductivity (with $\eta + \frac{1}{2} \in \mathbb{Z}$) depends on whether this level is full or empty [49, 50].

Likewise, a thin magnetic film lifts the degeneracy of Dirac points, which can also result in half-integer quantized Hall conductivity, $2\eta \in \mathbb{Z}$. This is called the anomalous quantum Hall effect [51]. Because the sign of σ_H depends on the direction of magnetization, there will be an one-dimensional "chiral" spin transport edge on the domain wall between two differently magnetized regions.

1.3.2 Topological Superconductors

Interesting physics can be generated by creating an interface between a TI and a superconductor (SC). Due to the well-known Holm-Meissner effect [52], the surface of a metal being in contact with a SC becomes superconducting as well, which can be explained by Cooper pairs tunneling to the surface of the SC. Interfaces to TIs are even more interesting, because of the special TI surface-states, which are protected by time reversal symmetry. In this case, the Cooper pairs on the surface will have even parity[8] and are not spin-degenerate. Similar experiments have already been done with graphene [53, 54], of course exhibiting double degeneracy. Corresponding experiments have not yet been carried out with TIs, because it is not known which materials will show the effect. A noble prediction for such material would also allow for the realization of Majorana fermions described in the next section.

[8] due to the π Berry phase

1.3.3 Majorana Fermions and Quantum Computation

Majorana fermions are quasi-particles, which can exist on the interface of SCs and TIs, but are not supported by either of those materials alone. Essentially, a Majorana fermion is "half of an ordinary Dirac fermion" [1] and it is its own anti-particle [55] (and thus charge-neutral). It follows non-Abelian statistics and its existence has long been theorized in particle physics (e.g., one neutrino may be Majorana fermion), but no experimental confirmation has been found yet. SC/TI interfaces now give new hope for a measurable realization of such a "half-electron". On top of that, quantum computers could make use of Majorana fermions, because they allow to store information non-locally ("in the topology") and thus avoid an accidentally collapse of the wave-function by self-measurement of the system. More specifically, robust computation is enabled by "topologically" protected states, which are insensitive to local perturbations.

1.3.4 Axion Electrodynamics and The Topological Magneto-electric Effect

Recently, Zhang developed the idea of axion electrodynamics [56] further and added a newly introduced topological term S_θ to the action of an electromagnetic ($\vec{E}$, $\vec{B}$) field:

$$S_\theta = \frac{\theta\alpha}{4\pi^2} \int_0^T \int_{\mathbb{R}^3} \vec{E} \cdot \vec{B} \; d^3r \, dt \; , \tag{1.3}$$

where $\alpha = \frac{e^2}{\hbar c}$ is the fine-structure constant. In the resulting topological field theory, time-reversal symmetry is not preserved in general. However, it is preserved for $\theta \in \{0, \pi\}$, marking two different topological classes (trivial and non-trivial). The new theory gives hope for a general understanding of topological phases and effects. It predicts a novel topological magneto-electric effect, where an applied electric field "generates a topological contribution to the magnetization in the same direction" [57].

Chapter 2

Theory

While the introductory chapter introduced topological insulators mostly chronologically, this chapter outlines the underlying theory of topological insulators in more detail. Further, this chapter mentions used definitions and describes computational methods used to generate the results of this thesis.

2.1 Density Functional Theory (DFT)

In order to provide adequate descriptions and predictions of (electronic) structures of atoms, molecules and solids, a quantum mechanical theory has to be used. In principle, all non-relativistic quantum effects of an N-particle system in volume $\mathcal{V} \subseteq \mathbb{R}^3$ can be described by the N-particle Schrödinger equation, which is a linear partial differential equation, whose solution is a set of wavefunctions $\Psi : \mathcal{V}^N \to \mathbb{C}$. All measurable quantities can be calculated out of Ψ. In the time-independent, stationary case with only Coulomb interaction between M nuclei with atom number Z_j at positions $\vec{R}_j$ and N electrons at positions $\vec{r_i}$, it can be written as follows:

$$\hat{\mathcal{H}}\,\Psi(\vec{r}_1,\ldots,\vec{r}_N) = E\,\Psi(\vec{r}_1,\ldots,\vec{r}_N) \tag{2.1}$$

$$\begin{aligned}
\hat{\mathcal{H}} &= \hat{T} + \hat{U} + \hat{V} \qquad (2.2)\\
\hat{T} &= -\frac{\hbar^2}{2m}\sum_{i=1}^{N}\nabla_i^2\\
\hat{U} &= \frac{e^2}{4\pi\varepsilon_0}\sum_{i=1}^{N}\sum_{j=i+1}^{N}\frac{1}{\|\vec{r_i}-\vec{r_j}\|}\\
\hat{V} &= -\frac{e^2}{4\pi\varepsilon_0}\sum_{i=1}^{N}\sum_{j=1}^{M}\frac{Z_j}{\left\|\vec{r_i}-\vec{R}_j\right\|} = \sum_{i=1}^{N}V(\vec{r_i})
\end{aligned}$$

For $N = 1$ and $M = 1$, i.e. the hydrogen atom ($U = 0$), an analytical solution is known. For larger systems, the solution has to be obtained numerically. However, the effort to directly calculate the N-particle wave-function scales exponentially with N and exceeds reasonable limits even for simple atoms. For example, for Si with 14 electrons and 10 mesh points in each dimension, this would require $10^{3 \cdot 14}$ data points just to store one Ψ. This exceeds the current approximated data capacity connected to the internet (500 exabytes [58]) by a *factor* of 10^{21}. A solution to this problem is provided by the Density Functional Theory (DFT), which states that all observable ground state (g.s.) properties of the system can be calculated (in principle exactly) out of the g.s. density $\rho : \mathcal{V} \to \mathbb{R}_{\geq 0}$.

$$\rho(\vec{r}) := N \int_{\mathcal{V}^{N-1}} |\Psi(\vec{r}, \vec{r_2}, \ldots, \vec{r_N})|^2 \, d^3 r_2 \ldots d^3 r_N \tag{2.3}$$

Hence,

$$\int_{\mathcal{V}} \rho(\vec{r}) d^3 r = N \ . \tag{2.4}$$

Since the results of this thesis were calculated with a DFT-based program (VASP [59,60]), the following sections will very briefly mention selected aspects of DFT, which are necessary for the understanding of the used computational method.

2.1.1 Hohenberg Kohn Theorem

Hohenberg and Kohn formulated the fundamental theorem of DFT [61], proving that if the g.s. is non-degenerate, any two distinct external potentials V_1, V_2 will always result in two distinct g.s. densities, $V_1 \neq V_2 \Rightarrow \rho_1 \neq \rho_2$. Thus, any density ρ_0 belonging to a g.s. can be mapped back uniquely to an external potential V. Since ρ_0 also yields N (by (2.4)), the kinetic energy operator $\hat{T}$ and the Coulomb interactions $\hat{U}$ of the above Hamilton operator (2.2) are completely defined. Thus, ρ_0 determines $\hat{\mathcal{H}}$ and consequently also the g.s. wave-function Ψ_0. Therefore, all observable g.s. properties $\langle \Psi_0 | \hat{A} | \Psi_0 \rangle$ are unique functionals $A[\rho_0]$ of the g.s. density, hence the name DFT.

A typical example is the g.s. energy $E_0 = \langle \Psi_0 | \hat{\mathcal{H}} | \Psi_0 \rangle$, which is now expressed as a sum of the external potential $V[\rho]$, the kinetic $T[\rho]$ and interaction

energy $U[\rho]$. Since $T[\rho]$ and $U[\rho]$ are V-independent, they can be combined into a universal functional $F[\rho] = T[\rho] + U[\rho]$, such that:

$$E_0[\rho] = F[\rho] + \int V(\vec{r})\,\rho(\vec{r})d^3r\ . \tag{2.5}$$

In practice, F is not known exactly and subject to approximations described below in section 2.1.3.

The Hohenberg-Kohn-theorem has been reviewed from a mathematical perspective [62, 63], taking special care about the definition spaces [64] of the mapping $V \leftrightarrow \hat{\mathcal{H}}$. It has further been generalized to cover degenerate ground states [65] and Hamilton operators involving a magnetic field [66]. Special treatment is needed when DFT is expanded to cover spin densities [67].

2.1.2 Self-Consistent Loop

In practice, the g.s. density is found iteratively by a self-consistent cycle introduced by Kohn and Sham [68]. To understand it, first $E[\rho]$ is rewritten as:

$$\begin{aligned} E_0[\rho] &= T_s[\rho] + U_H[\rho] + E_{xc}[\rho] + V[\rho] \\ T_s[\rho] &:= -\frac{\hbar^2}{2m}\sum_{i=1}^{N}\int_{\mathcal{V}} \overline{\Phi_i(\vec{r})}\nabla^2\Phi_i(\vec{r})d^3r\ , \\ U_H[\rho] &:= \frac{e^2}{2}\int_{\mathcal{V}}\int_{\mathcal{V}} \frac{\rho(\vec{r_1})\rho(\vec{r_2})}{\|\vec{r_1}-\vec{r_2}\|}d^3r_1 d^3r_2 \end{aligned} \tag{2.6}$$

where Φ_i are the single-particle orbitals of the *non*-interacting N-particle system. In essence, the approximations $T \approx T_s$ and $U \approx U_H$ were used, and the energy difference is covered by the exchange and correlation energy $E_{xc} = E_x + E_c$, $E_{xc} \leq 0$. There is a lower bound for E_{xc}[1]. To find the minimum energy, one calculates

$$\begin{aligned} 0 &= \frac{\delta E[\rho]}{\delta\rho(\vec{r})} \\ &= \frac{\delta T_s[\rho]}{\delta\rho(\vec{r})} + \frac{\delta U_H[\rho]}{\delta\rho(\vec{r})} + \frac{\delta E_{xc}[\rho]}{\delta\rho(\vec{r})} + \frac{\delta V[\rho]}{\delta\rho(\vec{r})} \\ &=: \frac{\delta T_s[\rho]}{\delta\rho(\vec{r})} + V_H(\vec{r}) + V_{xc}(\vec{r}) + V(\vec{r}) \end{aligned} \tag{2.7}$$

[1] Lieb and Oxford showed that $-1.679e^2\int_{\mathcal{V}}\rho(\vec{r})^{\frac{4}{3}}\,d^3r \leq E_{xc}[\rho] \leq 0$ [69, 70] for a known ρ.

Consequently, the density ρ of the interacting system can be calculated from the solution of the one-particle Schrödinger equation in the potential $V_s := V_H + V_{xc} + V$

$$\left[-\frac{\hbar^2}{2m}\nabla^2 + V_s(\vec{r})\right]\Phi_i(\vec{r}) = \varepsilon_i\Phi_i(\vec{r}) \tag{2.8}$$

by summing over the absolute squares of the single-particle orbitals Φ_i

$$\rho(\vec{r}) = \sum_{i=1}^{N} \alpha_i \left|\Phi_i(\vec{r})\right|^2 \ , \tag{2.9}$$

where $0 \leq \alpha_i \leq 1$ are the occupations.

Kohn and Sham introduced equation (2.8) and proposed the following scheme to find the ground state density:

1. Start with a random density ρ.
2. Calculate $V_s[\rho]$.
3. Solve (2.8).
4. Calculate the new density by (2.9). If it is very close to the old ρ, then stop; else loop again starting from step 2 with the new density.

At this point, only E_{xc} remains to be specified in order to find ρ_0. Possible approximations for E_{xc} are described in the next section.

2.1.3 Functionals

Well-known exchange and correlation functionals come in one of the following three forms:

$$E_{xc}^{LDA} = \int_{\mathcal{V}} f^{LDA}\left(\rho(\vec{r})\right) d^3r \tag{2.10}$$

$$E_{xc}^{GGA} = \int_{\mathcal{V}} f^{GGA}\left(\rho(\vec{r}), \nabla\rho(\vec{r})\right) d^3r \tag{2.11}$$

$$E_{xc}^{meta} = \int_{\mathcal{V}} f^{meta}\left(\rho(\vec{r}), \nabla\rho(\vec{r}), \tau(\vec{r})\right) d^3r \ , \tag{2.12}$$

where τ is the kinetic energy density:

$$\tau(\vec{r}) = \frac{\hbar^2}{2m}\left|\nabla\Psi(\vec{r})\right|^2 \ . \tag{2.13}$$

LDA

In the Local Density Approximation (LDA), E_x is given by:

$$E_x^{LDA}[\rho] = -\frac{3e^2}{4}\left(\frac{3}{\pi}\right)^{\frac{1}{3}} \int_{\mathcal{V}} \rho(\vec{r})^{\frac{4}{3}}\, d^3r \ . \tag{2.14}$$

$E_c^{LDA}[\rho] = \int_{\mathcal{V}} f_c^{LDA}(\rho(\vec{r}))\, d^3r$ and f_c^{LDA} is found by a parameterization of the results of intensive Quantum Monte Carlo simulations.

PBE

In 1996, Perdew, Burke and Ernzerhof (PBE) introduced a semi-local E_{xc}-functional [71,72], which can be considered as the most common one for solids within the Generalized Gradient Approximation (GGA). Just like LDA, PBE is free from "empirical" parameters and depends analytically on ρ and $\nabla\rho$. For its explicit form, see [71].

MBJLDA

In 2009 the new exchange potential MBJLDA was proposed [73]. It provides a semi-local and semi-empirical method, which was designed to accurately predict the band gap of semiconductors. However, it is not well suited to calculate effective masses (which are about 20-30% too high). Further, it is not derived from an exchange functional E_x such that $V_x^{MBJ} = \frac{\delta E_x}{\delta \rho}$ and therefore not well suited for structure optimization. Concerning band gaps and the overall band topology, MBJLDA seems to be as accurate as the computationally more expansive GW method. For a complete definition of MBJLDA, see appendix 5.2. For an overview of GW, see, e.g., [74].

2.2 Selected Aspects of Quantum and Solid State Physics

This section will briefly repeat some well-known concepts of quantum and solid state physics to reference them later in subsequent chapters.

2.2.1 The Concept of Band Structures

A solid can be modeled as an ideal crystal, which is defined by three linear independent *lattice vectors* $\vec{a_1}$, $\vec{a_2}$, $\vec{a_3} \in \mathbb{R}^3$ and a *atomic basis* consisting of a number of atoms (with their elements and positions). The atomic basis is appended to each lattice point spanned by all integer linear combinations of the lattice vectors. The parallelepiped spanned by the lattice vectors is called *primitive cell* and has the volume $\mathcal{V} = \det A$, where $A := (\vec{a_1}\ \vec{a_2}\ \vec{a_3})^T$.

One famous example of a lattice is the *zinc-blende* structure having the following lattice vectors and atomic basis (where a is the lattice constant):

$$\begin{aligned} \vec{a_1} &= \left(0, \frac{1}{2}, \frac{1}{2}\right) a \\ \vec{a_2} &= \left(\frac{1}{2}, 0, \frac{1}{2}\right) a \\ \vec{a_3} &= \left(\frac{1}{2}, \frac{1}{2}, 0\right) a \\ \vec{r_1} &= 0\,\vec{a_1} + 0\,\vec{a_2} + 0\,\vec{a_3} \\ \vec{r_2} &= \frac{1}{4}\,\vec{a_1} + \frac{1}{4}\,\vec{a_2} + \frac{1}{4}\,\vec{a_3} \end{aligned} \tag{2.15}$$

In this case, $\mathcal{V} = \frac{a^3}{4}$.

In order to solve the corresponding Schrödinger equation, a periodic one-electron system is considered and one makes the Bloch[2] ansatz for the wave functions

$$\Psi_{\vec{k}}(\vec{r}) = u_{\vec{k}}(\vec{r})\, e^{i\vec{k}\cdot\vec{r}}\,, \tag{2.16}$$

where the Bloch functions u are periodic under all lattice translations and $\vec{k}$ is the so-called *wave-vector*. All wave-vectors are translated back to the first

[2]Nobel price 1952

Brillouin zone, which is spanned by the following *reciprocal lattice vectors*:

$$\begin{aligned} \vec{b_1} &= \frac{2\pi}{\mathcal{V}}\, \vec{a_2} \times \vec{a_3}\ , \\ \vec{b_2} &= \frac{2\pi}{\mathcal{V}}\, \vec{a_3} \times \vec{a_1}\ , \\ \vec{b_3} &= \frac{2\pi}{\mathcal{V}}\, \vec{a_1} \times \vec{a_2}\ . \end{aligned} \tag{2.17}$$

The *band structure* consists of all bands $E_n(\vec{k})$ (possible energies for each $\vec{k}$) within the first Brillouin zone.

2.2.2 Time Reversal and Kramer's Theorem

This section states and proves Kramer's theorem in connection with time-reversal symmetry. While the form of the time-reversal operator Θ depends on the considered system, it is always bijective and anti-unitary, i.e. that for all wave functions Ψ and ϕ the following holds: $\langle \Theta\Psi | \Theta\phi \rangle := \overline{\langle \Psi | \phi \rangle} = \langle \phi | \Psi \rangle$. Hence, Θ is a non-linear (anti-linear) operator and $\Theta^2 = \pm 1$. Further, Θ can be written as combination of a unitary operator U and complex conjugation, $\Theta\phi = U\overline{\phi}$. Therefore, $\Theta\alpha = \overline{\alpha}\Theta$ for all $\alpha \in \mathbb{C}$, which are time-independent (or even under Θ - see appendix 5.3 for such properties).

Systems with half-integer total spin have the property that $\Theta^2 = -1$. In this case, all $\Psi \not\equiv 0$ are linearly independent to $\Theta\Psi$. If they were linearly dependent, then $\exists \alpha \in \mathbb{C} : \alpha\Psi = \Theta\,\Psi$ and $-1 \cdot \Psi = \Theta^2\Psi = \Theta\alpha\Psi = \overline{\alpha}\Theta\Psi = \overline{\alpha}\alpha\Psi = |\alpha|^2 \cdot \Psi$. However, there is no $\alpha \in \mathbb{C}$, such that $|\alpha|^2 = -1$.

Let $\overleftarrow{\mathcal{H}}$ be the time-reversal partner of the Hamilton operator $\mathcal{H}$ such that $\mathcal{H} = \Theta^{-1}\, \overleftarrow{\mathcal{H}}\, \Theta$. Suppose Ψ is an eigenfunction to the eigenvalue $E \in \mathbb{R}$ of $\mathcal{H}$, i.e., $\mathcal{H}\Psi = E\Psi$. Consequently, $\overleftarrow{\mathcal{H}}(\Theta\Psi) = \Theta\ \Theta^{-1}\overleftarrow{\mathcal{H}}\Theta\Psi = \Theta H\Psi = \Theta\, E\Psi = E(\Theta\Psi)$. In other words, $\Theta\Psi$ will be an eigenfunction of $\overleftarrow{\mathcal{H}}$ to the same eigenvalue E. Therefore all states of a time-reversal invariant system $\mathcal{H} = \overleftarrow{\mathcal{H}}$ for which $\Theta^2 = -1$ have an even degeneracy - this is known as *Kramer's theorem*.

In the absence of magnetic fields (or other time-reversal-breaking terms), $\mathcal{H}(-\vec{k})$ is the time-reversal partner of $\mathcal{H}(\vec{k})$. Therefore, the band structure is symmetric in this case: $E(\vec{k}) = E(-\vec{k})$. There are Time Reversal Invariant Momenta (TRIM), where $\vec{k} \hat{=} -\vec{k}$ (modulo a reciprocal lattice vector $\vec{G}$). While there are four TRIM points $\vec{k_a} = \frac{n_1\vec{b_1} + n_2\vec{b_2}}{2}$, $n_1, n_2 \in \{0, 1\}$ in 2D, there are eight

TRIM points in 3D: $\vec{k_a} = \frac{n_1\vec{b_1}+n_2\vec{b_2}+n_3\vec{b_3}}{2}$, $n_1, n_2, n_3 \in \{0, 1\}$. Due to Kramer's theorem, all bands at each TRIM point will have even degeneracy.

2.2.3 Strain Tensor and Elastic Constants

To describe linear deformations of the lattice, the strain tensor $\overleftrightarrow{\varepsilon} \in \mathbb{R}^{3\times3}$ can be used. The primitive cell A is linearly transformed by the symmetric[3] matrix $(\mathbb{I}_3 + \overleftrightarrow{\varepsilon})$. In Voigt notion, the strain tensor can be written as

$$\overleftrightarrow{\varepsilon} = \begin{pmatrix} e_1 & \frac{e_6}{2} & \frac{e_5}{2} \\ \frac{e_6}{2} & e_2 & \frac{e_4}{2} \\ \frac{e_5}{2} & \frac{e_4}{2} & e_3 \end{pmatrix} . \tag{2.18}$$

In expectation of a linear (force) response to deformations from the equilibrium (volume V_0), the total (binding) energy E is approximate as a multivariate polynomial of second order:

$$\begin{aligned} E^{harm}(\overleftrightarrow{\varepsilon}) &= E_0 + \frac{V_0}{2}\sum_{i=1}^{6}\sum_{j=1}^{6} e_i\, c_{ij}\, e_j \\ &= E_0 + \frac{V_0}{2}(c_{11}\, e_1^2 + 2c_{12}\, e_1\, e_2 + ...) \end{aligned} \tag{2.19}$$

The coefficients $c_{ij} = c_{ji}$ are called elastic constants and have the units of pressure.

2.2.4 Character Tables

A transformation which maps the ideal crystal bijectively onto itself is called a *symmetry operation*. Lattices have a finite number of symmetry operations, which form a group and can be partitioned into *equivalence classes*. The identity E is always in a class of its own. Mappings of the form $\vec{r} \mapsto M\vec{r}$ (M is a matrix) form a *point group*, while a *space group* is formed by mapping of the form $\vec{r} \mapsto M\vec{r} + \vec{b}$ ($\vec{b}$ is a vector). There are exactly 230 space groups in 3D if chiral copies are considered distinct, 219 otherwise.

A *representation* Γ_n is a mapping from group elements to square matrices with the property that for any two group elements the product of the representations is the representation of the product. A *character* is the trace of a

[3]Due to the symmetry $\overleftrightarrow{\varepsilon}_{ij} = \overleftrightarrow{\varepsilon}_{ji}$, this transformation does not involve rotations.

	E	$8\ C_3$	$3\ C_2$	$6\ I \times C_4$	$6\ I \times C_2'$
Γ_1	1	1	1	1	1
Γ_2	1	1	1	-1	-1
Γ_3	2	-1	2	0	0
Γ_4	3	0	-1	1	-1
Γ_5	3	0	-1	-1	1
Γ_6	2	1	0	$\sqrt{2}$	0
Γ_7	2	1	0	$-\sqrt{2}$	0
Γ_8	4	-1	0	0	0

Table 2.1: Double group character table of T_d, after [75].

representation. All representations in one equivalence classes have the same character (because the trace is invariant under similarity transformations). This motivates to formulate a character table with classes and presentations as columns and rows, respectively. When the spin orbit interaction is included, this group theory approach is slightly extended and the symmetries are properly described by the theory of *double groups*. See [75] for a comprehensive description of (double) group theory and its applications to physics.

To take an example, an face centered cubic (fcc) lattice is invariant under 48 symmetry operations. The zinc-blende structure adds two in-equivalent atoms to each fcc lattice point and therefore breaks the inversion and inversion-derived symmetries, reducing the number of symmetry operations to 24. The resulting point group of zinc-blende is called T_d (in Schönflies notation). After partitioning those 24 symmetry operations into 5 different (equivalence) classes, the double-group character table (table 2.1) can be constructed [75,76].

Representations Γ_n are often sorted by the character of the identity $\chi_{\Gamma_n}(E)$ (here: 1, 2, 3, 4), which is simply the dimensionality of the representation. Other than that, the author is not aware of any convention to sort the representations, which implies that, e.g., the labels Γ_6 and Γ_7 could be interchanged. Therefore, it is necessary to specify which character table was used when referring to a specific Γ_n; this work will later make use of the above table.

2.3 Topological Insulators

This section reviews selected aspects of the theory behind Topological Insulators. Since TIs are a subject of current research, the underlying theory is still developing, expanding and consolidating itself. Because of that, the purpose of this section is not to provide a complete, self-contained and logically coherent explanation of TIs, but merely to provide enough information to put this thesis into the context of current research. Where appropriate, references for further reading are provided.

In order to do so, this section firstly describes the topological argument of the IQHE. While it was published over 30 years ago, this argument has only recently gained attention, because it is referenced and reused in the context of the topological $\mathbb{Z}_2$ classification, described in the second section. Thereafter, the role of gap closings and finally the nature of the surface states is reviewed.

2.3.1 TKNN Argument

Although not explicitly mentioning the word "topology", one of the first papers to state that quantization of the IQHE conductivity can be understood by topological arguments was published in 1982 by Thousless, Kohmoto, Nightingale and Nijs (TKNN) [15]. They start with the Bloch ansatz $\Psi_{k_x,k_y} = u_{k_x,k_y} \exp(ik_x x + ik_y y)$ to obtain the 2D Hamilton operator defined (periodically) on a k_x-k_y-torus:

$$\mathcal{H}_{\text{TKNN}}(k_x, k_y) = \frac{\hbar^2}{2m}\left(-i\frac{\partial}{\partial x} + k_x\right)^2 + \frac{\hbar^2}{2m}\left(-i\frac{\partial}{\partial y} + k_y - \frac{e}{\hbar}Bx\right)^2 + U(x,y)\,, \tag{2.20}$$

where U is a lattice-periodic potential. Using the Kubo formula, they derive the Hall conductivity to be:

$$\sigma_H = \frac{ie^2}{2\pi h}\sum_{n=0}^{N_{occ}} \int_{BZ} dk_x\, dk_y \int_{A_0} dx\, dy \left(\frac{\partial \overline{u_n}}{\partial k_1}\frac{\partial u_n}{\partial k_2} - \frac{\partial \overline{u_n}}{\partial k_2}\frac{\partial u_n}{\partial k_1}\right)\,, \tag{2.21}$$

where $\int_{A_0}$ integrates over the 2D unit cell. This is rewritten using Stoke's theorem as:

$$\sigma_H = \frac{ie^2}{4\pi h}\sum_{n=0}^{N_{occ}} \oint_{\partial BZ} dk \int_{A_0} dx\, dy \left(\overline{u_n}\frac{\partial u_n}{\partial k_j} - \frac{\partial \overline{u_n}}{\partial k_j}u_n\right)\,, \tag{2.22}$$

which TKNN use to argue that the integral $\oint_{\partial BZ} dk$ can only evaluate to integer multiples of 2π, if the Bloch functions are defined continuously in the Brillouin zone.

In terms of mathematical topology, the integral (2.21) can also be understood as the so-called first Chern number of the U(1) fiber bundle built out of the Bloch functions $u_n(\vec{k})$, see [77] for a complete mathematical reference or [78] for the connection of Chern numbers to bulk and edge conductivity of the IQHE.

Another equivalent description was found by Berry [26] in 1984, based on the Berry connection $\vec{A}(\vec{k})$ and the Berry curvature $\vec{\mathcal{F}}(\vec{k})$.

$$\vec{A}(\vec{k}) = i \sum_{n=0}^{N_{occ}} \langle u_n(\vec{k}) | \nabla_{\vec{k}} | u_n(\vec{k}) \rangle \tag{2.23}$$

$$\vec{\mathcal{F}}(\vec{k}) = \nabla_{\vec{k}} \times \vec{A}(\vec{k}) \tag{2.24}$$

In this description, σ_H is simply[4]:

$$\sigma_H = \frac{ie^2}{2\pi h} \int_{BZ} dk_x \, dk_y \, \mathcal{F}_z(\vec{k}) \; . \tag{2.25}$$

Just like in the other cases, this integral only evaluated to multiples of an integer, such that $\sigma_H \cdot \frac{h}{e^2} \in \mathbb{Z}$. Similar considerations can be used to describe topological insulators, as will be seen in the next section.

2.3.2 Topological Z2 Classification

After calculating the band structure of a time reversal invariant system, it is clear whether the system has a band gap. If there is a gap, the system is either topologically trivial ($\nu = 0$) or non-trivial ($\nu = 1$). The $\nu = 1$ phase marks a topological insulator with the properties described in the introduction. This section should derive the formalism on how to calculate ν to tell the difference between those phases, following the ideas of Fu and Kane [27], which the

[4]This equation has a remarkable analogy to the topological formula of Gauß and Bonnet: for a surface S without a boundary (like a sphere or a torus), the integral over the local Gaussian curvature K of that surface gives: $\frac{1}{2\pi} \int_S K dA = 2(1-g) \in \mathbb{Z}$, where g is the genius of the surface (g=0 for a sphere and g=1 for a torus) [16].

author considers the most sound of several approaches to formulate the $\mathbb{Z}_2$ invariant [4, 6, 27, 57, 79–82].

In analogy to the charge polarization [83], Fu and Kane introduce "time reversal polarization". Therefore, charge polarization is reviewed briefly.

Charge Polarization

A one-dimensional system of length $L = aN_L$ is considered, where for the rest of this section the lattice constant a=1. The Bloch functions are written as:

$$\Psi_{n,k}(x) = \frac{1}{\sqrt{N_L}}\, e^{ikx}\, u_{n,k}(x)\ . \tag{2.26}$$

Now, *Wannier functions* associated with each unit cell of lattice vector R can be defined as:

$$w_{n,R}(r) = \frac{1}{2\pi}\int e^{ik(r-R)}\, u_{n,k}(r-R)\, dk\ . \tag{2.27}$$

One can now calculate the center of charge of those Wannier functions $\langle w_{n,R}|r|w_{n,R}\rangle$ and write the charge polarization P_ρ as the sum over the occupied bands associated with R=0:

$$P_\rho = \sum_{n=0}^{N_{occ}} \langle w_{n,0}|r|w_{n,0}\rangle\ . \tag{2.28}$$

By reintroducing the Berry connection, this is equivalent [27] to

$$P_\rho = \frac{1}{2\pi}\oint A(k)dk \tag{2.29}$$

Because the wave function $\Psi_{n,k}$ can be defined continuously over the Brillouin zone, the last integral is indeed a *close loop* from $k = -\pi$ to π.

While the polarization P_ρ is only defined up to a lattice vector, the difference $P_\rho(\xi_2) - P_\rho(\xi_1)$ between two adiabatically connected systems $\mathcal{H}(\xi_1)$ and $\mathcal{H}(\xi_2)$ is well defined (where ξ is a continuous parameter).

$$P_\rho(\xi_2) - P_\rho(\xi_1) = \frac{1}{2\pi}\left(\oint A(k,\xi_2)dk - \oint A(k,\xi_1)dk\right) \tag{2.30}$$

With the Berry curvature $\mathcal{F}_z$,

$$\mathcal{F}_z(k,\xi) = i\sum_{n=0}^{N_{occ}}\left(\frac{\partial}{\partial k}\langle u_{n,k,\xi}|\frac{\partial}{\partial \xi}|u_{n,k,\xi}\rangle - \frac{\partial}{\partial \xi}\langle u_{n,k,\xi}|\frac{\partial}{\partial k}|u_{n,k,\xi}\rangle\right) \tag{2.31}$$

$$= i\sum_{n=0}^{N_{occ}}\left(\langle\frac{\partial u_{n,k,\xi}}{\partial k}\mid\frac{\partial u_{n,k,\xi}}{\partial \xi}\rangle - \langle\frac{\partial u_{n,k,\xi}}{\partial \xi}\mid\frac{\partial u_{n,k,\xi}}{\partial k}\rangle\right)\ , \tag{2.32}$$

equation (2.30) can be rewritten [27] using Stokes' theorem:

$$P_\rho(\xi_2) - P_\rho(\xi_1) = \frac{1}{2\pi} \int_{\xi_1}^{\xi_2} \oint \mathcal{F}(k, \xi)\, dk\, d\xi \ . \tag{2.33}$$

Now a special case will be considered, where the system $\mathcal{H}(t)$ depends 2π-periodically on t, i.e.

$$\mathcal{H}(\xi) = \mathcal{H}(\xi + 2\pi) \ . \tag{2.34}$$

In this case, the charge "pumped" in one cycle $P_\rho(2\pi) - P_\rho(0)$ is the integral (2.33) over a torus (and equivalent to the first Chern number). For the same reasons as in equation (2.25), it will be an integer in general.

If the system fulfills the constraint that

$$\mathcal{H}(-\xi) = \Theta\, \mathcal{H}(\xi)\, \Theta^{-1} \ , \tag{2.35}$$

it follows that $\mathcal{F}(-k, -\xi) = -\mathcal{F}(k, \xi)$ and integral (2.33) is zero. Thus, there is no charge polarization after one cycle in such systems.

Time Reversal Polarization and Topological Invariant

Ideas presented above can now be used to define "time reversal polarization" and further the topological invariant ν of a 2D system $\mathcal{H}(k_x, k_y)$.

Let $\mathcal{H}(k_x, k_y)$ fulfill the time-reversal constraint 2.35 with $k = k_x$ and $\xi = k_y$. Since the Bloch functions $u(k_x, k_y)$ live on a torus, the periodicity of equation (2.34) is also fulfilled. Again, the total charge polarization P_ρ (2.33) is zero.

However, the picture becomes more interesting when spin-orbit interaction is added. In terms of the band structure of $\mathcal{H}(k_x, k_y)$, spin-orbit interaction splits each of the otherwise two-fold degenerate bands into a pair of two bands. Let $u^\uparrow$ and $u^\downarrow$ be a such pair of the corresponding Bloch states. Note that the labels $\uparrow$ and $\downarrow$ are used suggestively in this document, even though spin is not a good quantum number in the presence of spin-orbit interaction ($H_{SO} \propto \vec{L} \cdot \vec{S}$).[5] At each k, the $2N_{pairs}$ states can be grouped into pairs indexed by

[5]The labels $\uparrow$ and $\downarrow$ should only suggest that bands come in pairs, that each band is either of type $\uparrow$ or $\downarrow$, that the bands are split in energy by spin-orbit interaction, and that the quantities marked by $\uparrow/\downarrow$ are odd under $\mathcal{T}$, such that time-reversal flips both $\uparrow/\downarrow$ and the sign of $\vec{k}$. An advanced analogy would a property that is derived from a product of spin and momentum, like the spin helicity.

$\alpha = 1, \ldots, N_{pairs}$. Now, the time-reversal operator Θ flips momentum and spin at the same time. As an example, Θ could be defined as $\Theta u = e^{i\pi S_y/\hbar}\,\overline{u}$, where S_y is the spin operator. This means that $u_\alpha^\uparrow$ and $\Theta u_\alpha^\uparrow$ can only differ by a position-independent U(1) phase $\chi_\alpha(k)$.

$$u_\alpha^\uparrow(-k) = e^{i\chi_\alpha(k)}\ \Theta u_\alpha^\downarrow(k)\ . \tag{2.36}$$

With the property that $\Theta^2 = -1$ and knowning that Θ takes k to $-k$, this also means:

$$u_\alpha^\downarrow(-k) = -e^{i\chi_\alpha(-k)}\ \Theta u_\alpha^\uparrow(k)\ . \tag{2.37}$$

At the TRIM points (where k is equivalent to $-k$), the bands are degenerate.

This allows Fu and Kane to define the Berry connections $A^\uparrow$ and $A^\downarrow$ analogous to equation (2.23), but only involving the sum over the $u^\uparrow$ and $u^\downarrow$, respectively. Note that $A = A^\uparrow + A^\downarrow$. This results in the *partial polarizations* $P^\uparrow$ and $P^\downarrow$ analogous to equation (2.29). For $u^\uparrow$ bands along a k_y line in k-space, this is explicitly:

$$P^\uparrow(k_y) = \frac{1}{2\pi}\int_{-\pi}^{\pi} A^\uparrow(k_x, k_y)dk_x\ . \tag{2.38}$$

Due to the time-reversal constraint the above can also be expressed as an integral over the positive half space ($k_x > 0$) alone:

$$P^\uparrow(k_y) = \frac{1}{2\pi}\int_{0}^{\pi} \left(A^\uparrow(k_x, k_y) + A^\uparrow(-k_x, k_y)\right) dk_x\ . \tag{2.39}$$

While the charge polarization is $P\rho = P^\uparrow + P^\downarrow$, the time reversal polarization gets defined as $P_\Theta = P^\uparrow - P^\downarrow$. The topological invariant ν is then

$$\nu = P_\Theta(\pi) - P_\Theta(0) \bmod 2\ . \tag{2.40}$$

Because the gauge choice of $u_{n,k}$ will add an even number to ν [27], the latter is only defined mod 2.

Physical interpretation

Now, the connection between the above definitions and the physics of topological insulators should be explained.

Fu and Kane use a one-dimensional anti-ferromagnetic spin chain as analogy to describe a "$\mathbb{Z}_2$ adiabatic spin pump" [27], which should clarify the physical meaning of the above considerations. However, for the purpose of this thesis, the following hand-waving characterization will suffice: It should first be noted that equation (2.40) evaluates integrals along the lines from $k_x = 0$ to $k_x = \pi$ for both $k_y = 0$ and $k_y = \pi$, thus along two $\vec{k}$-lines between the four TRIM points. While the bands are two-fold degenerate at the TRIM points, spin-orbit interaction can be strong enough to separate a pair ($u_\alpha^\uparrow$ and $u_\alpha^\downarrow$) across the Fermi level along such a $\vec{k}$-line. This marks a "partner switching", which will also be referred to as "band inversion" below. Consequently, more bands of one kind ($\uparrow$ or $\downarrow$) can lie below the Fermi level along one $\vec{k}$-line and such a situation is then described by $\nu = 1$. Due to the $\mathcal{T}$-symmetry, this "inversion" occurs with exchanged $\uparrow/\downarrow$ labels along the $-\vec{k}$ line[6].

This point of view allows to understand that only bands in the range $E_F \pm \Delta_{SO}$ are important for the determination of the topological invariant ν (where Δ_{SO} is the maximum spin-orbit energy split of the bands) and why only the occupied bands are involved in the calculation of ν.

Further, it is intuitive to imagine that a second "inversion" would switch the partner back to normal, so that the band structure would again be equivalent to a trivial insulator. Therefore, ν is only defined mod 2 (an odd/even criterion).

In a $\mathcal{T}$-invariant system of a finite crystal, edge states reconnecting these two "$\mathcal{T}$ polarized" partners will then necessarily cross the Fermi level an odd number times on each boundary.

What remains to be done is count the number of band inversions, without knowing (a priori) which band is type $u^\uparrow$ or $u^\downarrow$. This can be done by beneficially combining $\uparrow$ and $\downarrow$ quantities to obtain formulas which no longer depend on both of those quantities explicitly.

[6] Thus, there is no net magnetization.

Equivalent Expressions of ν

After some algebra [27], Fu and Kane derive two expressions equivalent to (2.40) to calculate ν from the Bloch functions. The first uses the Berry curvature $\mathcal{F}$ additionally to the above Berry connection:

$$\nu = \frac{1}{2\pi}\left(\oint_{\partial\mathcal{B}^+} \vec{A}\cdot d\vec{k} - \int_{\mathcal{B}^+} \mathcal{F}_z\, dk_x\, dk_y\right) \mod 2\ , \tag{2.41}$$

where $\mathcal{B}^+$ is the positive half of the Brillouin zone (say, $k_y \geq 0$) and the above mentioned phase difference χ_α is fixed to 0, i.e., one needs to ensure that:

$$\begin{aligned} u_\alpha^\uparrow(-k_x,-k_y) &= \Theta\, u_\alpha^\downarrow(k_x,k_y) \\ u_\alpha^\downarrow(-k_x,-k_y) &= -\Theta\, u_\alpha^\uparrow(k_x,k_y) \end{aligned} \tag{2.42}$$

The second approach was already mentioned in the introduction: one chooses the Bloch functions $u_n(\vec{k})$ continuous throughout the Brillouin zone and computes the matrix $w_{mn}(k) = \langle u_m(-k)|\Theta|u_n(k)\rangle$ for all TRIM points of the system and used the Pfaffian[7] of w to get ν:

$$(-1)^\nu = \prod_{a=1}^{4} \frac{\sqrt{\det w(\vec{k_a})}}{\mathrm{Pf}\ w(\vec{k_a})} \tag{2.43}$$

In 3D, there is a simple generalization for each of the above formulas [84,85] and the topological index for a (strong) TI is called ν_0. Either, equation (2.43) is extended to all eight TRIM points, or, equation (2.41) is evaluated for both $k_z = 0$ and $k_z = \pi$ to subtract the obtained invariants z_0 and z_π:

$$\nu_0 = z_\pi - z_0 \mod 2\ . \tag{2.44}$$

If the crystal has inversion symmetry, there is a further simplification: ν_0 is the product of eight δ_a in 3D (or four δ_a in 2D) of the TRIM points $\vec{k_a}$ [5]. Each δ_a is a product of the parity $\mathcal{P}$ eigenvalues (± 1) at the corresponding TRIM point.

$$\delta_a = \prod_{n=1}^{N_{occ}} \langle u_{2n}(\vec{k_a})|\mathcal{P}|u_{2n}(\vec{k_a})\rangle \tag{2.45}$$

Since the degenerate u_{2n} and u_{2n-1} have the same parity eigenvalue, the product involves only half of the N_{occ} occupied bands.

[7] $(\mathrm{Pf\ M})^2 = \det \mathrm{M}$

2.3.3 Computing the Z2 Invariant

If the system does not have inversion symmetry (like zinc blende), equation (2.41) or (2.43) needs to be implemented. While equation (2.43) seems simpler, it only works if the wave functions are chosen continuous throughout the entire Brillouin zone. Although it is possible to solve this on a lattice version of the problem [79], it is hard in practice for realistic wave functions obtained by first-principle calculations [86].

Equation (2.41) is especially useful if routines for the calculation of $\vec{A}(\vec{k})$ and $\vec{\mathcal{F}}(\vec{k})$ are already available. Still, the gauge fixing condition (2.42) is not easy to implement, because wave functions for different $\vec{k}$ have a "random" local U(1) gauge. A description of a real-world example of an implementation can be found in [87][8].

In this section, an equivalent algorithm proposed by Yu et al. will be described which does not depend on any gauge-fixing condition [86]. The main idea of this algorithm is to keep track of the Wannier function centers of the occupied bands directly during one of the above mentioned adiabatic cycles (from $k_y = -\pi$ to π). The number of partner switchings (i.e., the number of band inversions) during this process, mod 2, defines the topological invariant ν. This is done by counting the winding number of the phases of the eigenvalues of a transfer matrix D (defined below). Proving the equivalence of this method to the above formulas is quite technically involved (see appendix of [86]) and therefore not repeated here. Instead, only the algorithm itself is stated.

The following procedure is done for both $k_z = 0$ and $k_z = \pi$.

Let there be N_{occ} (N_{occ} is even) occupied states at each $\vec{k}$-point in the Brillouin zone, so that three quantum numbers index each state $|n,\, k_x,\, k_y\rangle$. This allows to define a $N_{occ} \times N_{occ}$ matrix $F(k_x, k_y)$ containing the following overlap integrals,

$$\left(F(k_x, k_y)\right)_{mn} = \langle m,\, k_x,\, k_y \mid n,\, k_x + \Delta k_x,\, k_y \rangle \;, \tag{2.46}$$

where $\Delta k_x = \frac{2\pi}{N_x a}$ is the spacing of discrete grid containing N_x points and a is

[8] The appendix of [87] gives an idea on the amount of workload required for the implementation.

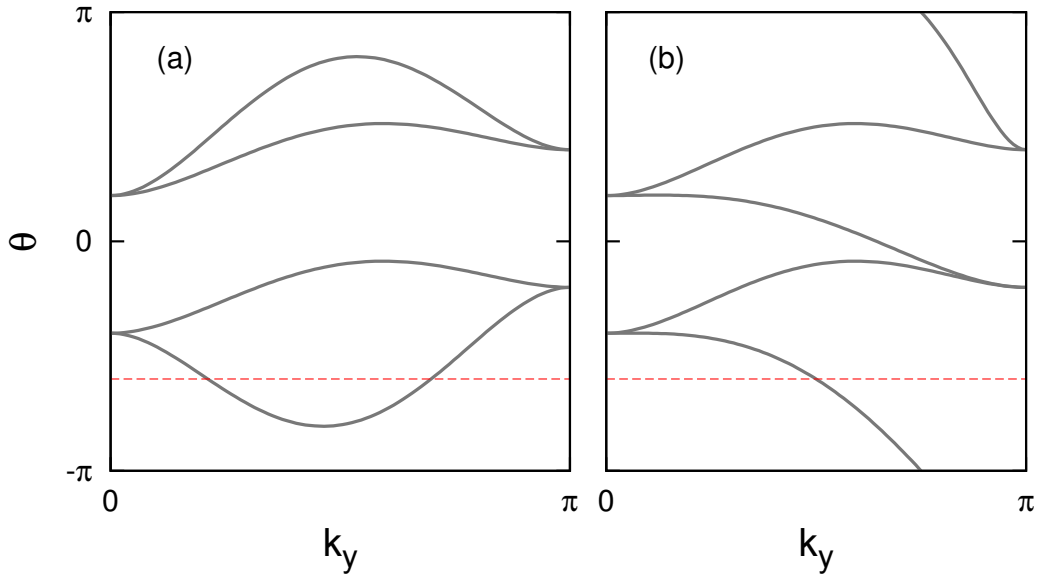

Figure 2.1: Sketch of the evolution of the $\theta_l(k_y)$ for two different cases, see equation (2.48). The dashed red line is crossed an (a) even and (b) odd number of times. Therefore, the topological invariant is 0 for (a) and 1 for (b). Note that $\theta^{(a)}(k_y) = \theta^{(b)}(k_y)$ for $k_y = 0$ and $k_y = \pi$. One can arbitrarily choose any horizontal reference line, except for a finite number of exceptions, where the reference line would coincide with a local extremum of the plotted curve.

the lattice constant. One can now calculate the complex $N_{occ} \times N_{occ}$ matrix

$$D(k_y) = \prod_{j=0}^{N_x-1} F\left(j\,\Delta k_x, k_y\right) \ , \tag{2.47}$$

which has N_{occ} complex eigenvalues

$$\lambda_l(k_y) = |\lambda_l(k_y)| e^{i\theta_l(k_y)} \ . \tag{2.48}$$

D is unitary and all $|\lambda_l(k_y)| = 1$ [86].

One now counts the number of crossings of any arbitrary horizontal (θ=const.) reference line with the evolution of the $\theta_l(k_y)$'s, mod 2. This results in the number z_0 or z_π, respectively. Finally, $\nu_0 = z_\pi - z_0 \mod 2 = z_\pi + z_0 \mod 2$, i.e. the system will be a in the phase of a trivial insulator ($\nu_0 = 0$) if the number of crossings is odd in both or even in both of the $k_z = 0$ and $k_z = \pi$ planes, and

a strong topological insulator ($\nu_0 = 1$) otherwise. The crossing is illustrated in Fig. 2.1.

Plausibly, the two planes ($k_z = 0$ and $k_z = \pi$) overall contain all eight TRIM points.

2.3.4 Band Inversion and Gap Closing

Topology studies properties invariant under smooth deformations. In particular, the topological invariant ν does not change under smooth deformations of the Bloch states $u(\vec{k})$, where a deformation is called smooth if it does not result in band touchings or crossings. Smooth deformation of the band structure is caused by smooth change of the lattice vectors or atom positions in the corresponding $\mathcal{T}$-invariant Hamilton operator. This allows to say that all those $\mathcal{T}$-invariant Hamilton operators are topologically equivalent that can be smoothly deformed into each other without closing their band gap. Hence, a gap closing is *necessary* for the change of the topological invariant. Murakami and Kuga claim that is also sufficient [88, 89]. Their proof differs between 2D from 3D cases and discusses systems with and without space inversion ($\mathcal{P}$) symmetry in each case. In the simplest case of a $\mathcal{T}$ and $\mathcal{P}$ invariant 2D system, it is shown that the gap can only close at a TRIM point. If m is the parameter controlling the deformation and causing the gap to vanish at $m = 0$, they show that up to linear order $\mathcal{H}_m(\vec{k_a}) = -\mathcal{H}_{-m}(\vec{k_a})$ (where $\mathcal{H}$ describes two valence and two conduction bands). They argue that the (two occupied) eigenfunctions u will therefore have opposite parity eigenvalues between $m < 0$ and $m > 0$. By equation (2.43), this is equivalent to a change of ν. The other cases (including 3D systems without inversion symmetry) are proven similarly, see [89] for details.

Results presented later in this thesis are in agreement with the above theorem, although they do not depend on them.

2.3.5 Surface States

It is quite remarkable that the band structure of the bulk material contains information to calculate ν and to determine if there will be gapless surface states. The connection can be understood by the "bulk-boundary correspondence" [1], which asserts that the number of gapless edge states at an interface is related to the difference in topological invariants of the regions in contact. If one accepts that the topological invariant cannot change as long as the band gap stays open, then it follows that any interface between systems with different topological invariants must necessarily have gapless edge states. This applies, e.g., to an interface between a strong TI ($\nu_0 = 1$) and the vacuum ($\nu_0 = 0$).

As a last point, the 2D band structure of the surface states should be discussed. A strong topological insulator always has an odd number of Dirac point on the surface [84]. In the simplest case of one Dirac point, the Hamilton operator is of the form

$$\mathcal{H}_{surface} = -i\hbar v_F \, \vec{\sigma} \cdot \vec{\nabla} \, , \tag{2.49}$$

where σ_i are the Pauli matrices. If the surface has mirror symmetry, this results in spin vectors "orthogonal" to $\vec{k}$, i.e. $\vec{S} \propto \vec{e_z} \times \vec{\sigma}$ [1].

$\mathcal{T}$-symmetry guarantees that in any case $\vec{S}(-\vec{k}) = -\vec{S}(\vec{k})$ is valid also for the surface states.

Chapter 3

Results for HgSe

This chapter presents the results of this work, which are published in parallel as paper [90]. Perhaps the most important outcome is the prediction that mercury selenide (HgSe) becomes a topological insulator under uniaxial strain. Therefore, the first section will describe the band structure of HgSe and compare DFT results with experimental data, both in equilibrium. Afterwards, the influence of both compressive and tensile strain is discussed. These results are then used to explain the topological phase transitions of HgSe and finally the surface states are shown, exhibiting the desired spin-polarization.

All these predictions have been made by the help of DFT calculations, for which parameters (like cut-off energies and $\vec{k}$-grid dimensions) are listed in the appendix 5.1.

3.1 Electronic Structure of HgSe in Equilibrium

Both experiment [91] and first-principle calculations [92] agree that in under ambient conditions[1], HgSe crystallizes in the zinc-blende structure, with atoms Hg ($Z_1 = 80$) and Se ($Z_2 = 26$). There is also approximate agreement on the lattice constant (see table 3.1).

However, the determination of the electronic (band) structure has not been without controversy between and within theory and experiment. Because agreement between theory and experiment is crucial to the nature and development of physics, the discrepancies should not be ignored here. The following paragraphs will therefore review not only undoubted results, but also elaborate possible sources of disagreement.

[1] i.e. pressure $p \approx 10^5$ Pa or smaller

Method	Ref.	a_0	V_0 / $\mathring{A}^3$	B_0 / GPa	B_0'
Experiment	[91]	6.084	56.30	58	
PBE	present and [92]	6.278	61.86	42	4.8
LDA	[92]	6.082	56.23	58	4.8

Table 3.1: Lattice constant a_0, equilibrium volume V_0, bulk modulus B_0 and its pressure derivative B_0' for different methods. Parameters found by a fit to an equation of state, see appendix 5.1.

3.1.1 States at the Γ-Point

There is agreement that the minimum gap occurs at the Γ point ($\vec{k_\Gamma} = \vec{0}$), for which group theory can predict symmetries of the states. Each allowed state at $\vec{k_\Gamma}$ can be classified into exactly one of the three double group representations Γ_6, Γ_7 and Γ_8, see section 2.2.4. The character of the identity $\chi_{\Gamma_n}(E)$ also marks to the degeneracy of any corresponding state. In agreement with Kramer's theorem (section 2.2.2), all $\chi_{\Gamma_n}(E)$ are even: two and four times degenerate states are allowed.

While many wave-functions are possible for each representation, in the present case of HgSe, the Γ_6 wave-functions are combinations of symmetric ("s-like") orbitals, whereas the Γ_7 and Γ_8 come from anti-symmetric ("p-like") orbitals. Group theory can predict allowed states and (dis)allowed level crossings; however, it can not predict energy values of those states. In turn, different computational methods and experiments are needed, which are covered in the next paragraphs, where the definitions $E_0 := E(\Gamma_6) - E(\Gamma_8)$ and $\Delta_{SO} := E(\Gamma_8) - E(\Gamma_7)$ are used.

3.1.2 Results of Previous Research

On the experimental side, early photoelectron spectroscopy (PES) investigations found an energy gap of 0.42 eV [93] on n-type HgSe (polar 001 surface with 2×2 reconstructions) in 1997. PES experiments measure the intensity of the emitted electron beam depending on energy, for different light frequencies. Afterwards, the results are fitted to a Gaussian model identifying peaks centered at different energies. Some of the peaks are derived from surface states;

they can be identified using the insensitivity to the measured $\vec{k}$-direction, and must be subtracted from the spectrum to obtain the bulk band structure. This procedure led to a picture where the experimental data was best described by a fit consisting of two bulk-peaks labeled Γ_6 and Γ_8, which were separated in energy by $E(\Gamma_6) - E(\Gamma_8) = 0.42 \pm 0.05\,\mathrm{eV}$. Since the Γ_6 peak only appeared for the photon energy of $h\nu = 12\,\mathrm{eV}$, it was concluded to be the conduction band minimum, thus, above the valance band maximum Γ_8.

However, in 2000, magneto-optical experiments "determined the band structure without the necessity of referring to a theoretical model" and "demonstrated unambiguously that HgSe is a semimetal [...] and not a semiconductor" [94]. The detailed analysis shows that Γ_7 is most likely lower in energy than Γ_6 (ordering $E(\Gamma_8) > E(\Gamma_6) > E(\Gamma_7)$). In contrast, an ingenious paper by Delin [95] pointed out that this conclusion is only valid within the model of symmetry-forbidden transitions between Γ_8 and Γ_7, which is not true, because both levels contain p and d states, such that the transition is indeed allowed.

Later PES experiments [96] (done on the non-polar 110-surface in 2001) could not confirm the positive value of E_0 and candidly noted that the resolution was too low to determine the ordering of the states at Γ.

From the above experiments, the compilation of results in [97] and references therein, the current major consensus appears to be that HgSe is indeed a semi-metal (i.e. a zero gap semi-conductor) and the most likely ordering is $E(\Gamma_8) > E(\Gamma_7) > E(\Gamma_6)$.

On the theoretical site, DFT and most GW calculations agree on the just mentioned ordering. While $\Delta_{SO} \approx 0.25\,\mathrm{eV}$ for all of LDA, PBE, GW, G′W′ and G_0W_0, the value for E_0 varies between $-0.40\,\mathrm{eV}$ for G′W′ and $-1.27\,\mathrm{eV}$ for LDA, as shown by table 3.2.

3.1.3 Basis for further Investigations

Figure 3.1 compares the calculated band structure of HgSe between PBE and an another functional, namely MBJLDA (described in section 2.1.3).

The most obvious difference is the value of E_0 (thus, the value of $E(\Gamma_6)$ relative to the Fermi level), which is around $-1.2\,\mathrm{eV}$ for PBE and $-0.23\,\mathrm{eV}$ for MBJLDA. The latter is in good agreement with GW calculations. In the

Method	Ref.	E_0	Δ_{SO}
QSGW	[98]	-0.11	0.27
MBJLDA	(present)	-0.23	0.20
h-QSGW	[98]	-0.32	0.27
G′W′	[99]	-0.40	0.23
G_0W_0	[98]	-0.45	0.24
GW	[100]	-0.58	0.32
PBE	(present)	-1.20	0.25
LDA	[100]	-1.27	0.23
Experiment	[97, 98]	≈-0.20	≈0.45

Table 3.2: Comparison of $E_0 := E(\Gamma_6) - E(\Gamma_8)$ and $\Delta_{SO} := E(\Gamma_8) - E(\Gamma_7)$ for different computational methods with experiment.

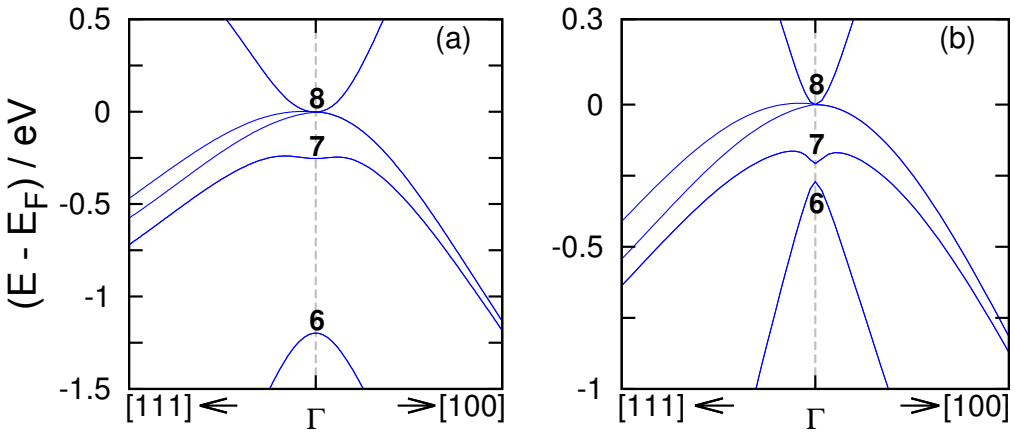

Figure 3.1: DFT band structures of HgSe in equilibrium for (a) PBE and (b) MBJLDA. The directions are given in Cartesian coordinates, such that [111] refers to $k_L = \frac{\pi}{a}(1,1,1)^\top$, where a is the equilibrium lattice constant.

following, PBE is used nevertheless, because of computational reasons[2] and because the most important feature in determining the evolution of topological changes is the ordering of the (frontier) bands at Γ, which is correctly predicted by PBE. Furthermore, it is argued below that the topological phase transition is caused by a band crossing of the frontier bands, independently from the band through Γ_6.

3.2 Electronic Structure of HgSe Under Strain

Strain changes the band structure of HgSe. In the following, three different directions of pressure were investigated:

- hydrostatic (uniform) pressure, keeping the cubic T_d symmetry,
- uniaxial strain along the [001] direction, i.e. one of the cubic axis, lowering the symmetry to the tetragonal D_{2d}, and
- uniaxial strain along the [110] direction, i.e. diagonal, lowering the symmetry to the orthorhombic $C_{2\nu}$.

It is known that uniaxial strain reduces the zinc-blende symmetry and causes zero-gap materials to open up a gap [101].

To quantify the pressure needed for such deformations, the elastic constants (see section 2.2.3) of the HgSe in zinc blende structure were calculated:

$$\begin{aligned} c_{11} = c_{22} = c_{33} &= 51.9 \text{ GPa} \\ c_{12} = c_{13} = c_{23} &= 37.7 \text{ GPa} \\ c_{44} = c_{55} = c_{66} &= 33.4 \text{ GPa} \end{aligned} \tag{3.1}$$

Apart from the symmetric partners $c_{ij} = c_{ji}$ of the above, the other c_{ij} are zero.

[2]The method used in this work to calculate the $\mathbb{Z}_2$ invariant relies on calculating overlap integrals of Bloch function $u_n(\vec{k})$, which must be chosen continuously throughout the Brillouin zone. Corresponding procedures are already implemented and well-tested for LDA and GGA functionals in the context of Berry-phase routines. However, this is not the case for GW or the semilocal meta-functional MBJLDA.

The next paragraphs will discuss the effects of those three deformations on the electronic band structure. Under uniaxial pressure, only distances orthogonal to the strain are varied, while the in-plane lattice constants are kept fixed. Therefore, strain can be defined by the strain direction and the value of $\varepsilon := \frac{V-V_0}{V_0}$. In the following, this value is denoted by $\varepsilon_{[001]}$ and $\varepsilon_{[100]}$, respectively. More specifically,

- under uniform pressure, the deformation is described by $e_1 = e_2 = e_3 = \sqrt[3]{\varepsilon} - 1$ and $e_4 = e_5 = e_6 = 0$,
- under uniaxial [001] strain, $e_1 = e_2 = e_4 = e_5 = e_6 = 0$ and $e_3 = \varepsilon_{[001]}$, and
- under uniaxial [110] strain, $e_3 = e_4 = e_5 = 0$, $e_1 = e_2 = \frac{\varepsilon_{[110]}}{2}$ and $e_6 = -\varepsilon_{[110]}$.

3.2.1 Hydrostatic Pressure

Uniform pressure keeps the T_d symmetry, including the four-fold generate Γ_8 state. Calculations have been carried out in a wide range $-30\% \leq \varepsilon \leq +30\%$, which covers very well the phase space in which the stable structure is zinc-blende: HgSe undergoes a phase transition to the cinnabar structure at $\varepsilon \approx -10\%$ compression (experiments: $\varepsilon = -9.0\%$ [102], $\varepsilon = -9.9\%$ [103]; theory: $\varepsilon^{PBE} = -11.0\%$, $\varepsilon^{LDA} = -13.9\%$ [92]), which corresponds to a uniform pressure of $p \approx 1\,\mathrm{GPa}$. In the zinc-blende phase, HgSe remains to be a semi-metal, which means that uniform pressure cannot cause a transition into the topological insulator phase, which would require a bulk band gap. In the cinnabar phase, HgSe does have a gap, but the calculation of the $\mathbb{Z}_2$ index suggests[3] that it is in the trivial insulator phase.

Therefore, the rest of this chapter will only be concerned with uniaxial strain breaking the T_d symmetry, in the hope to open up a "non-trivial" gap. It will turn out that HgSe indeed has a topologically non-trivial gap in some strain regions. To present this, first the effects of strain on the band structure are described independently from "topological" considerations. In the section following, the results for the calculation of the topological invariant are shown and finally the connection between the topological phase transitions and band structure changes is elaborated.

[3] After the transition, at $a = 5.5\,\text{Å}$, cinnabar-HgSe is topologically trivial. Since it is known from theory that topological phase transitions are always connected to gap closings (see section 2.3.4) and cinnabar is always gapped, it can be concluded that the whole cinnabar phase is topologically trivial - although that was not explicitly calculated.

3.2.2 Uniaxial Strain along [001]

Under uniaxial [001]-strain $\varepsilon_{[001]} = \frac{c-a}{a}$, the four-fold Γ_8 state splits in energy into two two-fold degenerate states, which can be labeled Γ_6 and Γ_7 in reference to the new character table of the double group of D_{2d} [75] (the Γ point has the full symmetry of that group). Figure 3.2 shows the band structures for (a) $\varepsilon_{[001]} = -5\%$ compression and (b) $\varepsilon_{[001]} = +3\%$ expansion.

Under compression, $E(\Gamma_6) < E(\Gamma_7)$, while expansion yields $E(\Gamma_6) > E(\Gamma_7)$. If the energy difference between those states is defined as $\Delta^{\Gamma}_{[001]} := E(\Gamma_6) - E(\Gamma_7)$, compression thus results in negative (or "inverted") splitting, $\text{sign}(\Delta^{\Gamma}_{[001]}) = \text{sign}(\varepsilon_{[001]})$.

Along the [001] strain direction (right hand site in Figure 3.2), the bands (Δ_5) stay doubly-degenerate (denoted by the green color), while the single-degenerate bands perpendicular to the strain (Σ_3, Σ_4) spin-split. Since the band-structure is point-symmetric to Γ (due to the time-inversion-symmetry), the green Δ_5 and blue Σ_4 show overall a "(reversed) camel-back" shape. The red Σ_3 exhibits a different shape and curvature than the Σ_4 band, resulting in a spin-dependent gap.

Under compression, the minimum gap $E_{gap} = 37\,\text{meV}$ occurs perpendicular to the strain (along the [110] direction), while under expansion an avoided crossing gap of $E_{gap} = 13\,\text{meV}$ occurs along the strain direction [001]. The Δ_5 bands belong to the $C_{2\nu}$ group, which does not allow for a crossing (which would be four-fold degenerate at one point).

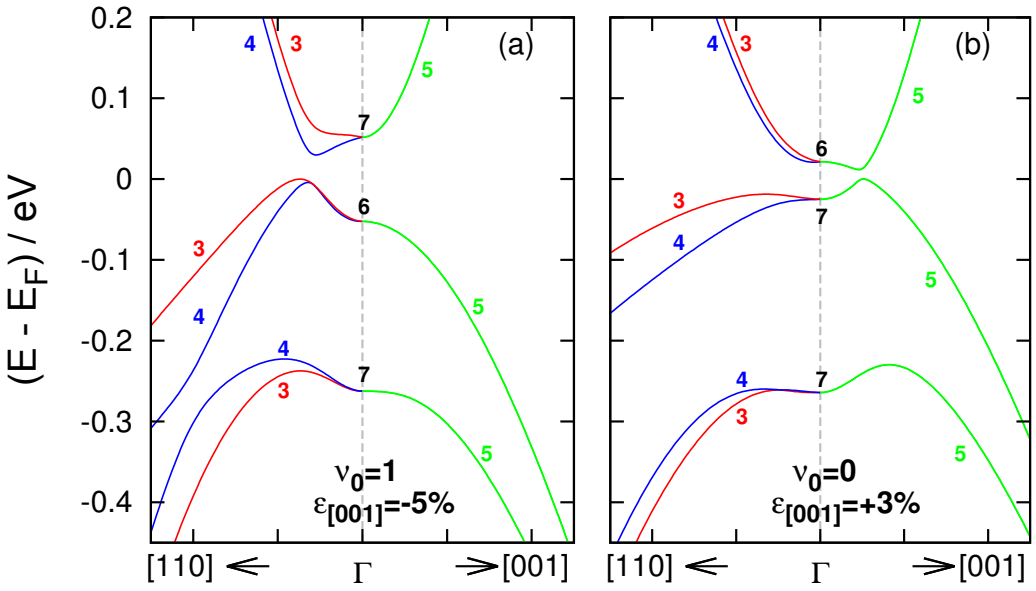

Figure 3.2: Band structure of HgSe under uniaxial strain along [001]. Shown directions are parallel [001] and perpendicular [110] to the strain. Red and blue lines are single-degenerate, while green bands are two-fold degenerate. (a) $\varepsilon_{[001]} = -5\%$ compression yields a energy gap of $E_{gap} = 37\,\mathrm{meV}$ in the non-trivial phase of a TI ($\nu_0 = 1$). (b) $\varepsilon_{[001]} = +3\%$ expansion yields a energy gap of $E_{gap} = 13\,\mathrm{meV}$ in the trivial phase of a normal band insulator. The numbers at Γ and next to the bands mark the corresponding representations.

3.2.3 Uniaxial Strain Along [110]

Under [110]-strain, the crystal reduces to the $C_{2\nu}$ symmetry. The corresponding band structure is shown for different strains in Figure 3.3.

Again, the strain opens up a gap in the vicinity of Γ due to the split of the zinc-blende Γ_8 into a conduction and valance state Γ_5. While the direct gap at Γ between those is in the order of magnitude $\Delta^{\Gamma}_{[110]} \approx 100\,\mathrm{meV}$, the fundamental gap occurs between bands perpendicular to the [110] strain. Compression (Fig. 3.3(a)) yields a similar picture as in the case of [001] strain. Uniaxial expansion, however, shows a more complex behavior in this case: first, a gap opens up for small strain $\varepsilon_{[110]} = +3\%$, (Fig. 3.3(b)), which closes for $\varepsilon_{[001]} = 5\% \ldots 6\%$ (Fig. 3.3(c)), and opens up widely for larger expansion (Fig. 3.3(d)).

	$\varepsilon_{[001]}$	E_{gap}	ν_0
(a)	-5%	31 meV	1
(b)	+3%	9 meV	1
(c)	+6%	0 meV	-
(d)	+8%	25 meV	0

Table 3.3: Strain strength, gap size and topological invariant for Figure 3.3.

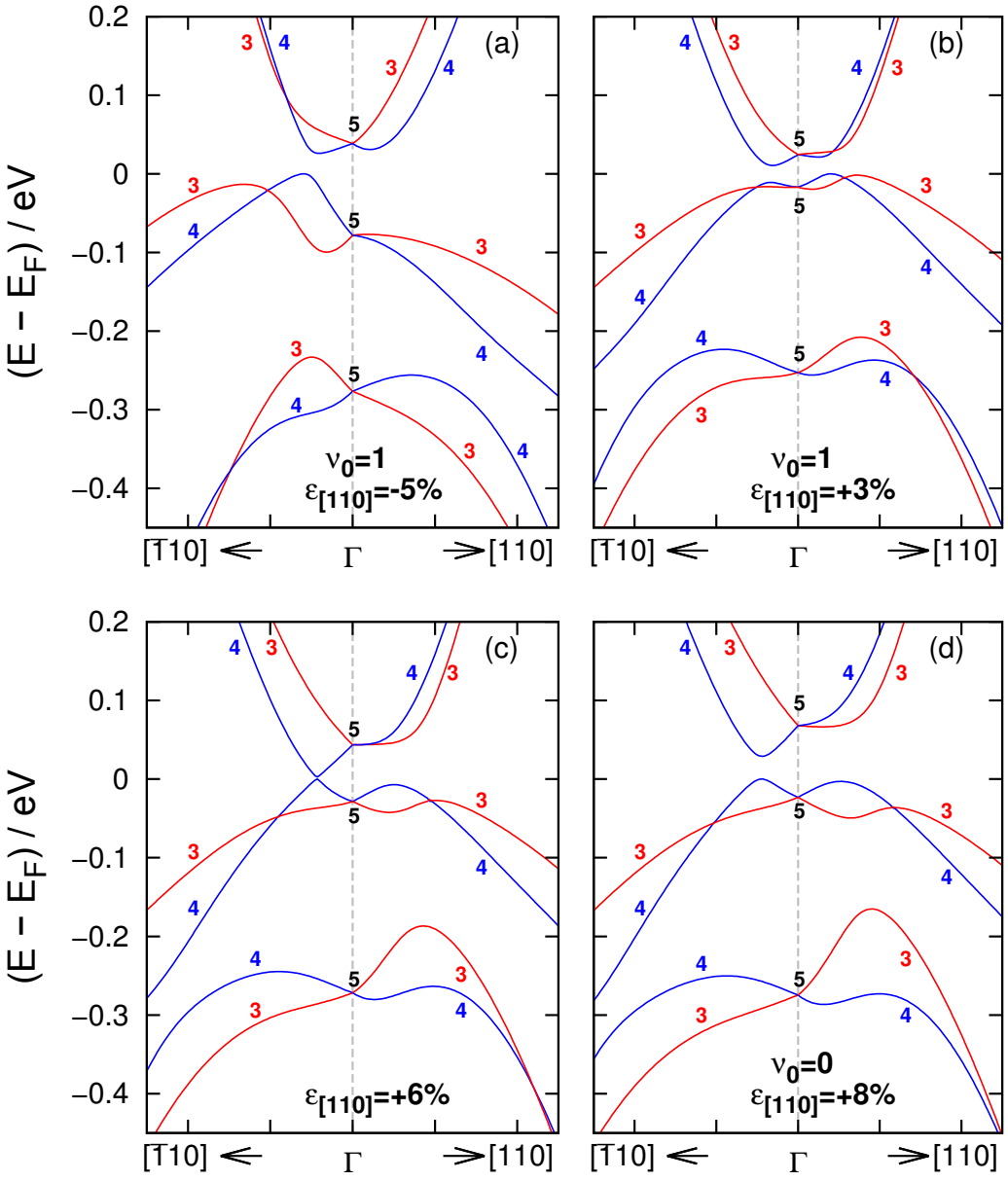

Figure 3.3: Band structure of HgSe under uniaxial strain along [110]. Shown directions are parallel [110] and perpendicular [$\bar{1}$10] to the strain. Red (Σ_3) and blue (Σ_4) lines are single-degenerate. (a) shows compression, while (b),(c) and (d) show expansion. There is a transition from the topological insulator phase $\nu_0 = 1$ in (b) to the trivial phase $\nu_0 = 0$ in (d), with the critical gapless transition point shown in (c). Values for E_{gap} are given in table 3.3. The numbers at Γ and next to the bands mark the corresponding representations.

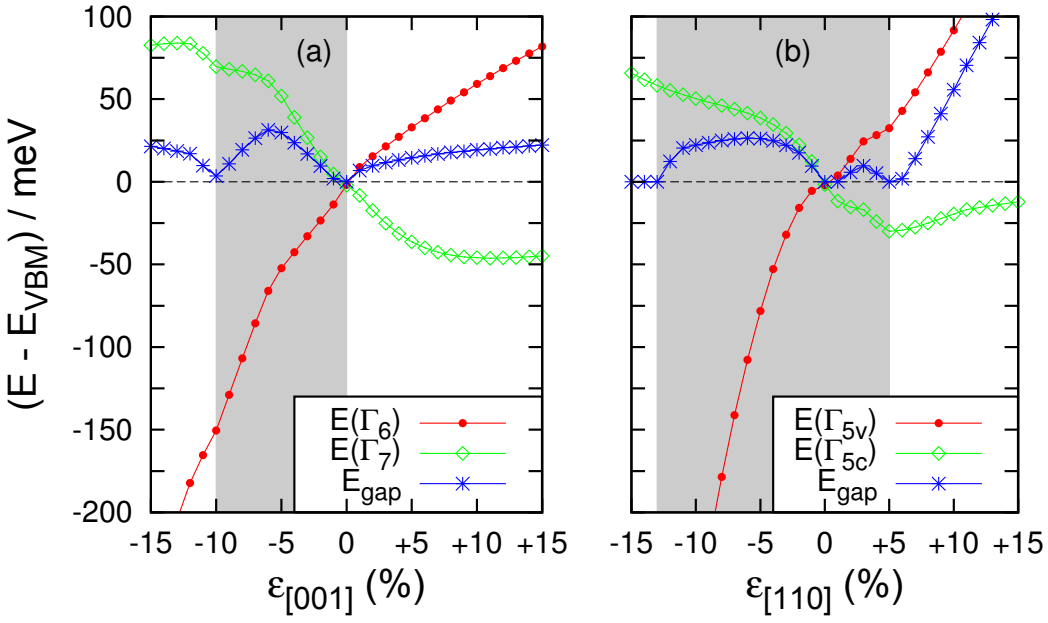

Figure 3.4: Energy levels $E_{\Gamma_n}(\varepsilon)$ of the highest occupied and lowest unoccupied state at Γ and fundamental energy gap $E_{gap}(\varepsilon)$ depending on strain. Energies are plotted relative to the valence band maximum (VBM) for strain along (a) [001] and (b) [110]. The range shaded in gray marks the topological non-trivial phase ($\nu_0 = 1$), while the white area is trivial $\nu_0 = 0$.

3.2.4 Evolution of the Energy Levels Under Strain

An overview of the energy levels and gap sizes is given for more strain values ($-15\% \leq \varepsilon \leq 15\%$) and both strain directions ([001] and [110]) in Figure 3.4. It can be seen that, since Γ is one point of the Brillouin zone, the gap between the highest occupied and lowest unoccupied states (red and green lines) is less or equal than the fundamental energy gap (blue line), $\left|\Delta^{\Gamma}\right| \leq E_{gap}$. While $\left|\Delta^{\Gamma}\right|$ increases monotonically under both compression and expansion, the E_{gap} shows non-monotonic behavior, which involves also gap-closing $E_{gap} = 0$ at some strain values. These critical strains also coincide with a slope change of the $E(\Gamma_n)$ lines and play an important role in the change of the topological phase, which will be discussed in the next section.

3.3 Topological Phase Transitions

Figure 3.4 has already marked the topological insulator phase by gray shaded areas, which has been done by calculating the topological invariant ν_0 for every of the plotted strains using the method described in section 2.3.3. On the basis of that figure, this section will firstly point out the connection between changes in ν_0 and the band structure and secondly try to provide an intuitive explanation for the observed behavior.

3.3.1 Change of the Topological Invariant For Different Strains

Changes in ν_0 happen at the critical strains where $E_{gap}(\varepsilon) = 0$, in agreement with the considerations of section 2.3.4, where it has been stated that the change of the topological invariant is always connected to a gap closing.

Under [001] compression, HgSe becomes a topological insulator and reaches its maximum bulk gap for $\varepsilon_{[001]} = -5\%$; the corresponding band structure has been plotted in Fig. 3.2(a). Stronger compression, however, results in a decreasing gap and a topological change back to the trivial phase after a gap closing at $\varepsilon_{[110]} = -10\%$. Expansion along [001] reproduces the same shape shown in Figure 3.2(b), where the minimum gap is formed by a avoided crossing of the Δ_5 bands. This gap is "trivial" and does not significantly increase with strain, as shown on the right hand site of Figure 3.4(a).

Compression along [110] (left hand side of Fig. 3.4(b)) yields a similar behavior as in the [001] case, i.e. a transition to the TI phase and a change back to the trivial phase for larger strain ($\varepsilon_{[110]} = -13\%$). The highest achievable bulk band gap $E_{gap} = 31\,\text{meV}$ occurs again at $\varepsilon_{[110]} = -5\%$, with a slightly lower value than in the [001] case. In contrast, the [110] expansion (right hand side of Fig. 3.4(b)) differs from the [001] case: Small tensile strain opens up a small "non-trivial" gap, which closes again for $\varepsilon_{[110]} = +5\% \ldots + 6\%$. Further expansion opens up a much larger gap, but unfortunately in a topologically trivial phase.

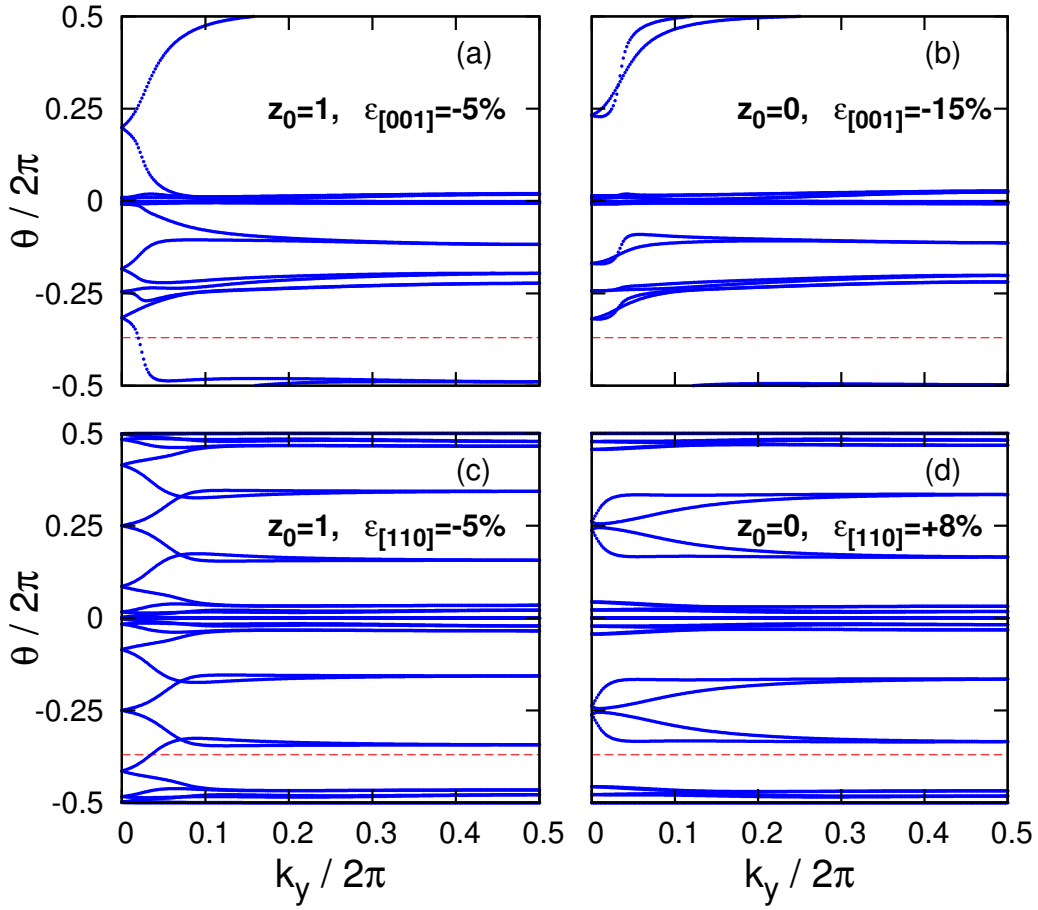

Figure 3.5: Examples of the evolution of the Wannier function centers in the $k_z = 0$ plane, calculated by the method described in section 2.3.3. Any horizontal, arbitrary reference line (like the dashed red line) is crossed an odd number of times in (a) $\varepsilon_{[001]} = -5\%$ and (c) $\varepsilon_{[110]} = -5\%$, and an even number of times in (b) $\varepsilon_{[001]} = -15\%$ and (d) $\varepsilon_{[110]} = +8\%$. Hence, the topological index z_0 is 1 for (a) and (c), and 0 for (b) and (d). In all cases, the corresponding $z_\pi = 0$. Consequently, $\nu_0 = z_0$.

3.3.2 Possible Explanation for the Topological Phase Transitions

Based on observations of the band structures for many different strains (including the ones shown in Figures 3.2 and 3.3), this section aims to provide an intuitive explanation of the connection between topological phase transitions and changes in the band structure. In order to do so, the mechanism of band inversion is schematically drawn in Figure 3.6. Starting from the zero-gap material with the Γ_8 state of zinc-blende, there are two ways in which uniaxial strain can change the band structure.

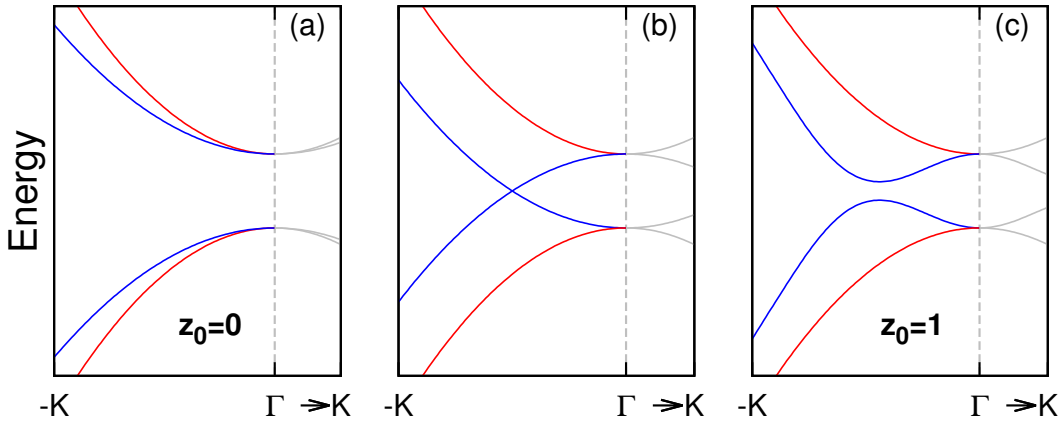

Figure 3.6: Schematic of the strain-induced evolution of the band structure along an arbitrary direction ($\Gamma \leftrightarrow \pm K$) in the $k_z = 0$ plane, where the spin-split bands are marked in red and blue. (a) The strain splits the originally four-fold degenerate frontier bands at Γ in electrons and holes bands, which does not involve any band crossing and hence the bulk system is in a topologically trivial phase with $z_0 = 0$. (b) Band inversion of one of the spin-split bands (blue) at the critical strain. (c) Odd number (one) of band inversions for one of the bands (blue) at a larger strain giving rise to a band gap opening. Consequently, conduction and valence band show an (inverse) camel-back-shape along the $\Gamma \leftrightarrow \pm K$ direction, bringing the system in the topologically non-trivial phase ($z_0 = 1$). Note that the inverted bands have both positive and negative curvature.

The first is to simply separate the electron and hole states in energy as shown in Fig. 3.6(a). This does not involve any band inversion and marks the phase of a trivial insulator ($z_0 = 0$ for the $k_z = 0$ plane). An example for this behavior can be seen along the [110] direction in Fig. 3.2(b).

The second possibility to connect the bands is shown in Fig. 3.6(b). One can imagine that strain pushes the bands into each other, causing a band overlap. After the critical transition point where the gap closes, a gap is opened up again (Fig. 3.6c), e.g., by crystal field splitting. Due to the spin orbit coupling, an odd number (one) of bands is inverted in this case, leading to a topologically non-trivial situation ($z_0 = 1$), where the bands are "knotted". An example for it is shown along the [110] direction in Fig. 3.2(a). At first glance, the Δ_5 bands along the [001] direction in 3.2(b) also seem to exhibit a camel-back shape. However, the Δ_5 bands are doubly degenerated, so that there is an even number (two) of band inversions. Likewise, the [110] case can be explained: there is one band inversion in Fig. 3.3(b). Increasing strain pulls the conduction Σ_4 band down, until it reaches the critical point in Fig. 3.3(c), reassembling the situation sketched in Fig. 3.6(b). After that transition, the system has experienced a second band inversion and is therefore "unknotted" back into a topologically trivial case ($z_0 = 0$) in Fig. 3.3(d).

So far, only band-inversions around the Γ point, i.e. in the $k_z = 0$ plane, have been discussed. Fortunately, the conduction and valance bands at the other seven TRIM points are well separated in energy ($\approx 2\,\mathrm{eV}$) for all strains, so that spin orbit coupling is not strong enough to cause any further band inversions in the $k_z = \pi$ plane.
Therefore, $z_\pi = 0$ and consequently $\nu_0 = (z_\pi - z_0) \mod 2 = z_0$.

Thus, the topological phases could be completely identified just by the shape of the bulk band structure. However, this method is cumbersome and has to be carried out very carefully, because all different $\vec{k}$-directions have to be considered and the inverted bands have to be identified correctly. Therefore, the more reliable method remains to be the calculation of the topological invariant ν_0 (which was used for the shading in Fig. 3.4).

3.4 Surface States

Surface states are phenomenologically the most desired property of TIs. While the calculation of the $\mathbb{Z}_2$ invariant is sufficient to guarantee for their existence in the case of $\nu_0 = 1$, a direct calculation of a multi-layered slab can provide additional assurance and more information. Here, a slab was built out of 21 atomic (110)-planes to form a non-polar surface, which was uniaxially strained by $\varepsilon_{[110]} = -10\%$. The resulting band structure is shown in Figure 3.7 and contains both bulk and surface states. In order to identify the states present on the surface, the Kohn-Sham wave-function $\Phi^{KS}_{\vec{k}}$ was projected onto hydrogen-like spherical harmonics centered on each of the surface atoms. Summing over those contributions $\langle nlm\vec{k}|\Phi^{KS}_{\vec{k}}\rangle$ from the two top and two bottom atomic layers allows to determine a percentage of "surfaceness" at each $\vec{k}$-point of the 2D Brillouin zone, which was color-coded in Fig. 3.7 (method similar to [104]). Two different Dirac-cones (from top and bottom surface) are superimposed, such that the Kramers-degenerate Dirac point is four-fold degenerate and $\approx$ 50 meV below the Fermi energy.

Figure 3.8 shows another important feature of TIs: the spin vectors[4] $\langle\vec{S}\rangle$ for circles of $\vec{k}_{\|}$-points in the 2D Brillouin zone. The blue circles correspond to (almost) constant energy contours and the red circle overlaps with the Fermi energy. As expected, the surface states are spin-polarized $\langle\vec{S}(-\vec{k})\rangle = -\langle\vec{S}(\vec{k})\rangle$. In agreement with theoretical considerations and findings for other known TI materials, the spin is almost normal to the in-plane momentum, $(\langle S_x\rangle, \langle S_y\rangle) \perp (k_x, k_y)$.

[4]The spin vectors result from a non-collinear spin calculation, i.e. every spin direction (S_x, S_y, S_z) is associated with its own spin density, such that the DFT program uses four densities in total (the fourth is the charge density).

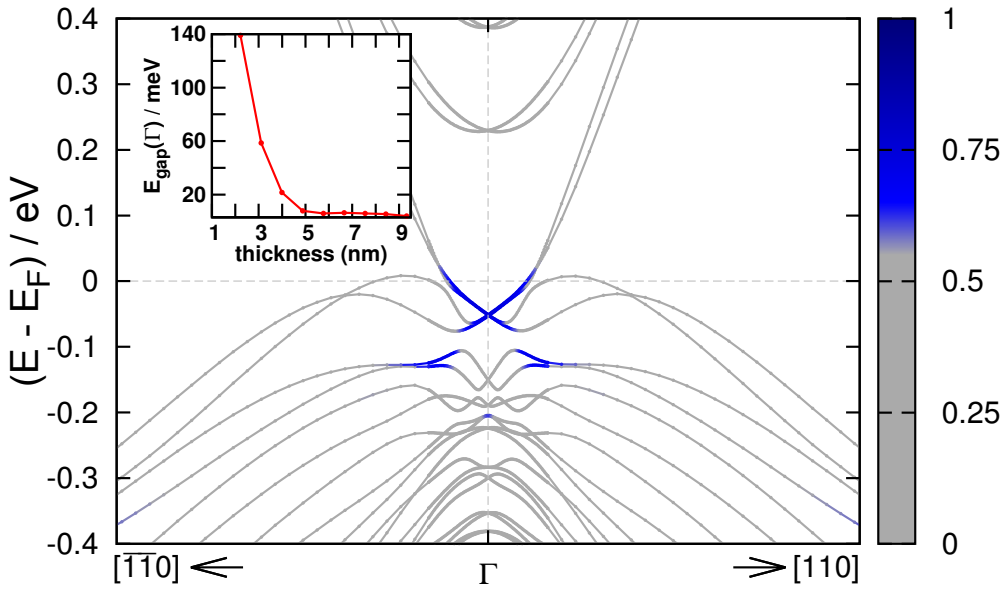

Figure 3.7: Band structure of the (110) HgSe surface under a [110] uniaxial compressive strain ($\epsilon_{[110]} = -10\%$) along the $\pm$[110] directions in the 2D Brillouin zone, showing two Dirac-cones (from top and bottom surfaces) at Γ, 52 meV below the Fermi energy. The gray and blue colored bands correspond to bulk- and surface-derived states, where the latter are associated with the two top-most and bottom-most atomic layers.

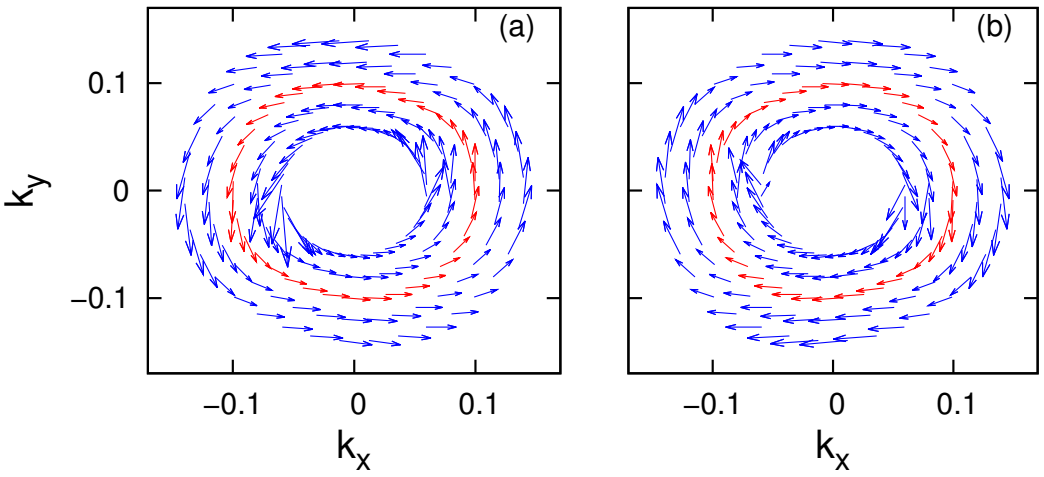

Figure 3.8: Spin vectors along constant energy contours in the 2D Brillouin zone of the uniaxially strained (110) HgSe surface from Fig. 3.7 within an energy of $E_F \pm 25\,\text{meV}$, projected onto the (a) top and (b) bottom surfaces, respectively. All states shown are above the Dirac point and the red arrow contours denote the spin polarization vector of states at E_F. The closer to Γ, the lower the energy of the state. k_x and k_y are in multiples of $\frac{2\pi}{a}$.

Chapter 4

Conclusions

4.1 Summary

In summary, the main purpose of this work was to show the effect of uniaxial strain on the electronic structure of mercury selenide. While HgSe is a zero-gap semiconductor in equilibrium, strain necessarily opens up a gap. Some gapped states are topologically equivalent to normal insulators, but in specific strain regions discussed above, the system is in the phase of a topological insulator. In this phase, the largest band gap of 37 meV occurs at -5% (under uniaxial compression along one of the cubic axes). Surface states were calculated showing spin-polarized linear dispersion. Computations of the topological $\mathbb{Z}_2$ invariant show critical topological phase transition points at strains where the band gap is zero. A band inversion picture could be established that might allow to identify the topological phase by the shape of the band structure around the TRIM points alone.

Spin-orbit interaction is usually said to invert s and p states, leading to "negative gap" materials, which are effectively TIs. Contrary to this commonly accepted statement, this work showed that both topologically trivial and non-trivial phases can occur while the s-like Γ_6 state is below the the p-like Γ_7 and Γ_8. Therefore, this criterion might be necessary, but it is not sufficient. Further, calculations (not shown here) reveal that s-derived bands are below p-bands even without spin-orbit coupling. It is therefore advisable to always calculate the $\mathbb{Z}_2$ invariant, which is the most reliable criterion.

4.2 Critique

Naturally, all predictions presented in this work are only certain within the physical models which they are based upon, as it can always be doubted in how far those models will apply to reality. In order to place this work in its scientific context, this section therefore elaborates some of the possible points of criticism:

- *DFT* can (in principle exactly) predict ground-state properties based on an one-electron ground-state density, but DFT does not guarantee correctness of exited states. It is common to identify the Kohn-Sham eigenvalues with the actual band structure and since the used $\mathbb{Z}_2$ criterion is defined for (non-interacting) one-particle systems, it was straightforward to follow this tradition. Strictly speaking, one has consequently no guarantee that the subsequently calculated topological $\mathbb{Z}_2$ invariant is correct. Shortcomings of DFT in connection with TIs have also been mentioned in [105].

  On top of that, the exact universal DFT functional is unknown, so that in practical implementations approximative functionals are used, here the GGA functional *PBE*.

  However, DFT successfully describes many solid state properties like geometries, lattice constants and binding energies within a relative error of a few percent. Together with the theoretical considerations of the gap-closing mechanism, the effect is believed to be realized in experiments, perhaps with slightly different values for energy gap E_{gap} and strain value.

- Neither the *influence of relaxation* with respect to the atomic degrees of freedom nor the *influence of crystal defects* was studied. However, it is proven that no time-reversal-invariant (i.e. non-magnetic) perturbation can change the topological phase as long as the bulk gap is not closed. Therefore, these influences are negligible for small strain and sufficiently clean samples.

- The results assume a mono-crystal, while real-world HgSe is likely to be *polycrystalline*, resulting in a mixture of different strain directions.

On the other hand, it was shown above that compression in different directions results in a topologically non-trivial phase. A mixture of strain directions is therefore likely to be non-trivial, as well.

- Methods for the *practical application of strain* were not discussed. Strained HgTe was grown in a quantum wells structure "sandwiched" between several CdTe layers. Following this idea, a CdSe/HgSe quantum well could be grown experimentally. However, the mismatch in lattice constant between CdSe and HgSe is relatively low, resulting in a presumably small strain effect. Mechanical strain might be considered as alternative.

  In that context, it should also be noted that the lattice constant normal to the strain was fixed during the calculations, while it would be more realistic to relax it (in a good approximation, conserving the volume).

- Within the topological phase, only a *small gap* $E_{gap} \approx 35\,\mathrm{meV}$ was achieved. For practical applications, conduction should only be allowed on the surface - preventing surface electrons to be scattered back into bulk states. In order to do so, the HgSe sample should be cooled down to $3 \cdot k_B T < E_{gap} \approx 3\,k_B \cdot 135\,\mathrm{K}$, which is reachable by nitrogen cooling.

- Finally, *numerical errors* are possible, mainly due to the choice of numerical precision, cut-off parameters and $\vec{k}$-grid resolution. However, these errors are presumed to be small in comparison to systematic errors, e.g., from the PBE functional.

4.3 Outlook

Finally, some perspective for future research shall be mentioned:

- We are looking forward to an *experimental test* of the predictions, currently planned by the group around Y. P. Chen at the Purdue University.
- Future research could re-calculate the results of this work with *different DFT functionals* or by means of *GW calculations*. Also, different strain scenarios could be calculated concerning other strain directions and $\frac{a}{c}$-ratios, e.g., expanding a while decreasing c.
- The two-atom model of HgSe can provide another *simple theoretical test case* for the ongoing research about Topological Insulators.
- Uniaxial strain appears to become a theme in the search for new TIs. There is hope that the results and mechanisms presented in this thesis inspire other researches in their search for next-generation TIs.

Chapter 5

Appendix

5.1 DFT Parameters

The Vienna Ab initio Simulation Package (VASP) [59, 60] was used for all calculations, which uses the projected augmented wave (PAW) approach [106] and norm-conserving pseudo-potentials. While the electron configuration of Hg is [Xe] $6s^2\,4f^{14}\,5d^{10}$, for Se it is [Ar] $4s^2\,3d^{10}\,4p^4$. For Hg, the 6s and 5d electrons were treated explicitly; for Se, the 4s and 4p electrons. The GGA exchange functional is PBE [71] (see section 2.1.3). Spin-orbit coupling was included in all self-consistent and band-structure calculations. All self-consistent bulk calculations used a Monkhorst-Pack mesh [107] with 11×11×11 $\vec{k}$-points; for the surface (slab) calculation, it was 7×7×1. A plane-wave basis was used with an energy cut-off of 550 eV for the bulk and 450 eV for the surface calculations. The equilibrium volume $V_0 = 61.86$ Å (i.e. $a_0 = 6.278$ Å) was found by a fit to the Murnaghan equation of state [108]:

$$E(V) = E_0 - \frac{B_0 V_0}{B_0' - 1} + \frac{B_0 V}{B_0'}\left(\frac{\left(\frac{V_0}{V}\right)^{B_0'}}{B_0' - 1} + 1\right) . \tag{5.1}$$

The non-polar (110) surface is modeled by a periodic slab consisting of 21 atomic layers with a 12 Å thick vacuum region separating the periodic slabs.

5.2 MBJLDA

The Modified Becke-Johnsen (MBJ) potential $V_x^{MBJ}[\rho]$ is an exchange potential [73], based on the previous work of Becke and Johnsen (BJ) [109]. To define it, the following non-linear equation is first solved for each $x(\vec{r}), \vec{r} \in \mathcal{V}$

$$\frac{x(\vec{r})\, e^{-2x(\vec{r})/3}}{x(\vec{r}) - 2} = 4\pi^{\frac{2}{3}} \frac{\rho(\vec{r})^{\frac{5}{3}}}{\nabla^2\rho(\vec{r}) - 4\gamma\tau(\vec{r}) + \frac{\gamma}{2}\frac{(\nabla\rho(\vec{r}))^2}{\rho(\vec{r})}} \tag{5.2}$$

and then used to calculate the Becke-Roussel potential V_x^{BR}:

$$V_x^{BR}(\vec{r}) = -\left[\frac{8\pi\rho(\vec{r})}{e^{-x(\vec{r})}}\right]^{\frac{1}{3}} \cdot \left(1 - e^{-x(\vec{r})} - \frac{1}{2}x(\vec{r})e^{-x(\vec{r})}\right) \tag{5.3}$$

The above is now used to define the Modified Becke Johnsen (MBJ) potential V_x^{MBJ}, which is added as a purely local term to the Kohn Sham potential V_s:

$$V_x^{MBJ} = c\, V_x^{BR}(\vec{r}) + (3c - 2)\frac{1}{\pi}\sqrt{\frac{5\,\tau(\vec{r})}{6\,\rho(\vec{r})}} \tag{5.4}$$

While $c = 1$ recovers the original BR potential, the experimental band gap can be reproduced by fitting to an optimal c_{opt}; the gap increases monotonically with c. Tran and Blaha find that for solids with small band gaps $1.1 \leq c_{opt} \leq 1.3$, while for large gaps $1.4 \leq c_{opt} \leq 1.7$. They looked at c_{opt} for several materials and found that it correlates with the average kinetic energy density and chose therefore:

$$c = \alpha + \beta\left(\frac{1}{\mathcal{V}}\int_{\mathcal{V}} \frac{|\nabla\rho(\vec{r})|}{\rho(\vec{r})} d^3r\right)^{\frac{1}{2}} \quad . \tag{5.5}$$

A fit to the experimental values of the band gap for 23 materials (from Ge over GaAs to solid Ne) leads $\alpha = -0.012$ and $\beta = 1.023\sqrt{a_{\text{Bohr}}}$. The value for c can be found self-consistently and depends (non-locally) on the density in the entire unit cell.

5.3 Properties Odd and Even under $\mathcal{P}$ and $\mathcal{T}$

	even under $\mathcal{P}$	odd under $\mathcal{P}$
even under $\mathcal{T}$	mass m, charge q, energy E, electrostatic potential ϕ	position $\vec{x}$, acceleration $\vec{a}$, force $\vec{F}$, electric field $\vec{E}$, electric induction $\vec{D}$
odd under $\mathcal{T}$	time t, angular momentum $\vec{L}$, magnetic field $\vec{B}$, magnetizing field $\vec{H}$	velocity $\vec{v}$, current density $\vec{j}$, vector potential $\vec{A}$, Pointing vector $\vec{S}$

Table 5.1: Some classical properties under $\mathcal{P}$ and $\mathcal{T}$ symmetry.

Bibliography

[1] M. Z. Hasan and C. L. Kane. Colloquium: Topological insulators. *Rev. Mod. Phys.*, **82**; pp. 3045–3067, 2010. 13, 17, 25, 45

[2] X.-L. Qi and S.-C. Zhang. The quantum spin Hall effect and topological insulators. *Physics Today*, **63**, no. 1; pp. 33–38, 2010. 13

[3] C. L. Kane and E. J. Mele. Quantum Spin Hall Effect in Graphene. *Phys. Rev. Lett.*, **95**; p. 226801, 2005. 13, 17, 18

[4] C. L. Kane and E. J. Mele. Z_2 Topological Order and the Quantum Spin Hall Effect. *Phys. Rev. Lett.*, **95**; p. 146802, 2005. 13, 17, 37

[5] L. Fu and C. L. Kane. Topological insulators with inversion symmetry. *Phys. Rev. B*, **76**; p. 045302, 2007. 13, 20, 22, 41

[6] J. E. Moore and L. Balents. Topological invariants of time-reversal-invariant band structures. *Phys. Rev. B*, **75**; p. 121306, 2007. 13, 37

[7] B. A. Bernevig, T. L. Hughes and S.-C. Zhang. Quantum Spin Hall Effect and Topological Phase Transition in HgTe Quantum Wells. *Science*, **314**, no. 5806; pp. 1757–1761, 2006. 13, 22

[8] M. König, S. Wiedmann, C. Brüne, A. Roth, H. Buhmann, L. W. Molenkamp, X.-L. Qi and S.-C. Zhang. Quantum Spin Hall Insulator State in HgTe Quantum Wells. *Science*, **318**, no. 5851; pp. 766–770, 2007. 13, 22

[9] D. Hsieh, D. Qian, L. Wray, Y. Xia, Y. S. Hor, R. J. Cava and M. Z. Hasan. A topological Dirac insulator in a quantum spin Hall phase. *Nature*, **452**, no. 7190; pp. 970–974, 2008. ISSN 0028-0836. 13, 21, 22

[10] Y. Xia, D. Qian, D. Hsieh, L. Wray, A. Pal, H. Lin, A. Bansil, D. Grauer, Y. S. Hor, R. J. Cava and M. Z. Hasan. Observation

of a large-gap topological-insulator class with a single Dirac cone on the surface. *Nature Physics*, **5**, no. 6; pp. 398–402, 2009. ISSN 1745-2473. 13, 22

[11] H. Zhang, C.-X. Liu, X.-L. Qi, X. Dai, Z. Fang and S.-C. Zhang. Topological insulators in Bi2Se3, Bi2Te3 and Sb2Te3 with a single Dirac cone on the surface. *Nature Physics*, **5**, no. 6; pp. 438–442, 2009. ISSN 1745-2473. 13, 22

[12] F. D. M. Haldane. Model for a Quantum Hall Effect without Landau Levels: Condensed-Matter Realization of the "Parity Anomaly". *Phys. Rev. Lett.*, **61**; pp. 2015–2018, 1988. 13

[13] A. K. Geim and K. S. Novoselov. The rise of graphene. *Nature Mater*, **6**, no. 3; pp. 183–191, 2007. ISSN 1476-1122. 13

[14] K. v. Klitzing, G. Dorda and M. Pepper. New Method for High-Accuracy Determination of the Fine-Structure Constant Based on Quantized Hall Resistance. *Phys. Rev. Lett.*, **45**; pp. 494–497, 1980. 13, 14

[15] D. J. Thouless, M. Kohmoto, M. P. Nightingale and M. den Nijs. Quantized Hall Conductance in a Two-Dimensional Periodic Potential. *Phys. Rev. Lett.*, **49**; pp. 405–408, 1982. 13, 14, 35

[16] J. E. Avron, D. Osadchy and R. Seiler. A Topological Look at the Quantum Hall Effect. *Physics Today*, **56**, no. 8; pp. 38–42, 2003. 13, 36

[17] E. H. Hall. On a New Action of the Magnet on Electric Currents. *American Journal of Mathematics*, **2**, no. 3; pp. pp. 287–292, 1879. ISSN 00029327. 14

[18] M. Janssen, O. Viehweger, U. Fastenrath and J. Hajdu. *Introduction to the Theory of the Integer Quantum Hall Effect*. VCH Verlagsgesellschaft mbH, 1994. ISBN 3-527-29267-5. ISBN 3-527-29209-8. 14, 16

[19] C. Kane and J. Moore. Topological insulators. *Physics World*, **24**; pp. 32–36, 2011. 15, 18

[20] D. C. Tsui, H. L. Stormer and A. C. Gossard. Two-Dimensional Magnetotransport in the Extreme Quantum Limit. *Phys. Rev. Lett.*, **48**; pp. 1559–1562, 1982. 16

[21] X.-G. Wen. Topological Orders and Chern-Simons Theory in strongly correlated quantum liquid. *International Journal of Modern Physics B*, **05**, no. 10; pp. 1641–1648, 1991. 16

[22] X.-G. Wen. An introduction of Topological Orders, 2002. Http://dao.mit.edu/ wen/topartS3.pdf. 16

[23] X.-G. Wen. Topological orders and edge excitations in fractional quantum Hall states. *Advances in Physics*, **44**, no. 5; pp. 405–473, 1995. 16

[24] H. Nielsen and M. Ninomiya. The Adler-Bell-Jackiw anomaly and Weyl fermions in a crystal. *Physics Letters B*, **130**, no. 6; pp. 389 – 396, 1983. ISSN 0370-2693. 17

[25] S. Chandrasekharan and U.-J. Wiese. An Introduction to Chiral Symmetry on the Lattice. Http://arxiv.org/abs/hep-lat/0405024. 17

[26] M. V. Berry. Quantal phase factors accompanying adiabatic changes. *Proc. R. Soc. Lond. A*, **392**; pp. 45–47, 1984. 17, 36

[27] L. Fu and C. L. Kane. Time reversal polarization and a Z_2 adiabatic spin pump. *Phys. Rev. B*, **74**; p. 195312, 2006. 19, 36, 37, 38, 39, 40, 41

[28] D. Hsieh, Y. Xia, L. Wray, D. Qian, A. Pal, J. H. Dil, J. Osterwalder, F. Meier, G. Bihlmayer, C. L. Kane, Y. S. Hor, R. J. Cava and M. Z. Hasan. Observation of Unconventional Quantum Spin Textures in Topological Insulators. *Science*, **323**, no. 5916; pp. 919–922, 2009. 21, 22

[29] D. Hsieh, L. Wray, D. Qian, Y. Xia, J. H. Dil, F. Meier, L. Patthey, J. Osterwalder, G. Bihlmayer, Y. S. Hor, R. J. Cava and M. Z. Hasan. Direct observation of spin-polarized surface states in the parent compound of a topological insulator using spin- and

angle-resolved photoemission spectroscopy in a Mott-polarimetry mode. *New Journal of Physics*, **12**, no. 12; p. 125001, 2010. 21, 22

[30] F. WanXiang and Y. YuGui. Three-dimensional topological insulators: A review on host materials. *Science China Physics, Mechanics and Astronomy*, **55**, no. 12; 2199, 2012. 21

[31] C. Brüne, C. X. Liu, E. G. Novik, E. M. Hankiewicz, H. Buhmann, Y. L. Chen, X. L. Qi, Z. X. Shen, S. C. Zhang and L. W. Molenkamp. Quantum Hall Effect from the Topological Surface States of Strained Bulk HgTe. *Phys. Rev. Lett.*, **106**; p. 126803, 2011. 22

[32] W. Feng, W. Zhu, H. H. Weitering, G. M. Stocks, Y. Yao and D. Xiao. Strain tuning of topological band order in cubic semiconductors. *Phys. Rev. B*, **85**; p. 195114, 2012. 22

[33] H. Guo, K. Sugawara, A. Takayama, S. Souma, T. Sato, N. Satoh, A. Ohnishi, M. Kitaura, M. Sasaki, Q.-K. Xue and T. Takahashi. Evolution of surface states in $Bi_{1-x}Sb_x$ alloys across the topological phase transition. *Phys. Rev. B*, **83**; p. 201104, 2011. 22

[34] W. Zhang, R. Yu, H.-J. Zhang, X. Dai and Z. Fang. First-principles studies of the three-dimensional strong topological insulators Bi 2 Te 3 , Bi 2 Se 3 and Sb 2 Te 3. *New Journal of Physics*, **12**, no. 6; p. 065013, 2010. 22

[35] Y. L. Chen, J. G. Analytis, J.-H. H. Chu, Z. K. Liu, S.-K. K. Mo, X. L. Qi, H. J. Zhang, D. H. Lu, X. Dai, Z. Fang, S. C. Zhang, I. R. Fisher, Z. Hussain and Z.-X. X. Shen. Experimental realization of a three-dimensional topological insulator, Bi2Te3. *Science*, **325**, no. 5937; pp. 178–181, 2009. ISSN 1095-9203. 22

[36] D. Hsieh, Y. Xia, D. Qian, L. Wray, F. Meier, J. H. Dil, J. Osterwalder, L. Patthey, A. V. Fedorov, H. Lin, A. Bansil, D. Grauer, Y. S. Hor, R. J. Cava and M. Z. Hasan. Observation of Time-Reversal-Protected Single-Dirac-Cone Topological-Insulator States in Bi_2Te_3 and Sb_2Te_3. *Phys. Rev. Lett.*, **103**; p. 146401, 2009. 22

[37] D. Xiao, Y. Yao, W. Feng, J. Wen, W. Zhu, X.-Q. Chen, G. M. Stocks and Z. Zhang. Half-Heusler Compounds as a New Class of Three-Dimensional Topological Insulators. *Phys. Rev. Lett.*, **105**; p. 096404, 2010. 22

[38] W. Feng, D. Xiao, Y. Zhang and Y. Yao. Half-Heusler topological insulators: A first-principles study with the Tran-Blaha modified Becke-Johnson density functional. *Phys. Rev. B*, **82**; p. 235121, 2010. 22

[39] S. Chadov, X. Qi, J. Kübler, G. H. Fecher, C. Felser and S. C. Zhang. Tunable multifunctional topological insulators in ternary Heusler compounds. *Nature Mater*, **9**, no. 7; pp. 541–545, 2010. ISSN 1476-1122. 22

[40] H. Lin, L. A. Wray, Y. Xia, S. Xu, S. Jia, R. J. Cava, A. Bansil and M. Z. Hasan. Half-Heusler ternary compounds as new multifunctional experimental platforms for topological quantum phenomena. *Nature Mater*, **9**, no. 7; pp. 546–549, 2010. ISSN 1476-1122. 22

[41] W. Al-Sawai, H. Lin, R. S. Markiewicz, L. A. Wray, Y. Xia, S.-Y. Xu, M. Z. Hasan and A. Bansil. Topological electronic structure in half-Heusler topological insulators. *Phys. Rev. B*, **82**; p. 125208, 2010. 22

[42] C. Shekhar, S. Ouardi, G. H. Fecher, A. K. Nayak, C. Felser and E. Ikenaga. Electronic structure and linear magnetoresistance of the gapless topological insulator PtLuSb. *Applied Physics Letters*, **100**, no. 25; 252109, 2012. 22

[43] N. P. Butch, P. Syers, K. Kirshenbaum, A. P. Hope and J. Paglione. Superconductivity in the topological semimetal YPtBi. *Phys. Rev. B*, **84**; p. 220504, 2011. 22

[44] W. Feng, D. Xiao, J. Ding and Y. Yao. Three-Dimensional Topological Insulators in I-III-VI_2 and II-IV-V_2 Chalcopyrite Semiconductors. *Phys. Rev. Lett.*, **106**; p. 016402, 2011. 22

[45] S. Chen, X. G. Gong, C.-G. Duan, Z.-Q. Zhu, J.-H. Chu, A. Walsh, Y.-G. Yao, J. Ma and S.-H. Wei. Band structure engineering of multinary chalcogenide topological insulators. *Phys. Rev. B*, **83**; p. 245202, 2011. 22

[46] Y. J. Wang, H. Lin, T. Das, M. Z. Hasan and A. Bansil. Topological insulators in the quaternary chalcogenide compounds and ternary famatinite compounds. *New Journal of Physics*, **13**, no. 8; p. 085017, 2011. 22

[47] S. Manipatruni, D. E. Nikonov and I. A. Young. Circuit Theory for SPICE of Spintronic Integrated Circuits, 2011. Online http://arxiv.org/abs/1112.2746. 23

[48] C. W. Sandweg, Y. Kajiwara, A. V. Chumak, A. A. Serga, V. I. Vasyuchka, M. B. Jungfleisch, E. Saitoh and B. Hillebrands. Spin Pumping by Parametrically Excited Exchange Magnons. *Phys. Rev. Lett.*, **106**; p. 216601, 2011. 23

[49] R. Jackiw. Fractional charge and zero modes for planar systems in a magnetic field. *Phys. Rev. D*, **29**; pp. 2375–2377, 1984. 24

[50] R. Jackiw. Erratum: Fractional charge and zero modes for planar systems in a magnetic field. *Phys. Rev. D*, **33**; pp. 2500–2500, 1986. 24

[51] O. Pankratov. Supersymmetric inhomogeneous semiconductor structures and the nature of a parity anomaly in (2+1) electrodynamics. *Physics Letters A*, **121**, no. 7; pp. 360 – 366, 1987. ISSN 0375-9601. 24

[52] R. Holm and W. Meissner. Messungen mit Hilfe von flüssigem Helium. XIII. *Zeitschrift für Physik*, **74**; pp. 715–735, 1932. ISSN 0044-3328. 24

[53] P. Ghaemi and F. Wilczek. Near-zero modes in superconducting graphene. *Physica Scripta*, **2012**, no. T146; p. 014019, 2012. Also on http://arxiv.org/abs/arXiv:0709.2626. 24

[54] D. L. Bergman and K. Le Hur. Near-zero modes in condensate phases of the Dirac theory on the honeycomb lattice. *Phys. Rev. B*, **79**; p. 184520, 2009. 24

[55] C. Nayak, S. H. Simon, A. Stern, M. Freedman and S. Das Sarma. Non-Abelian anyons and topological quantum computation. *Rev. Mod. Phys.*, **80**; pp. 1083–1159, 2008. 25

[56] F. Wilczek. Two applications of axion electrodynamics. *Phys. Rev. Lett.*, **58**; pp. 1799–1802, 1987. 25

[57] X.-L. Qi, T. L. Hughes and S.-C. Zhang. Topological field theory of time-reversal invariant insulators. *Phys. Rev. B*, **78**; p. 195424, 2008. 25, 37

[58] R. Wray. Internet data heads for 500bn gigabytes. Online on guardian.co.uk, 2009. Http://www.guardian.co.uk/business/2009/may/18/digital-content-expansion. 27

[59] G. Kresse and J. Hafner. Ab initio molecular dynamics for liquid metals. *Phys. Rev. B*, **47**; pp. 558–561, 1993. 27, 69

[60] G. Kresse and J. Furthmüller. Efficient iterative schemes for *ab initio* total-energy calculations using a plane-wave basis set. *Phys. Rev. B*, **54**; pp. 11169–11186, 1996. 27, 69

[61] P. Hohenberg and W. Kohn. Inhomogeneous Electron Gas. *Physical Review*, **136**; pp. 864–871, 1964. 27

[62] E. H. Lieb. Density functionals for coulomb systems. *International Journal of Quantum Chemistry*, **24**, no. 3; pp. 243–277, 1983. ISSN 1097-461X. Theorem 3.4 proves the existence of densities that have no corresponding ground-state wave-function. 28

[63] M. Levy. Electron densities in search of Hamiltonians. *Phys. Rev. A*, **26**; pp. 1200–1208, 1982. Counter-example for V-representability given in section V. 28

[64] J. E. Harriman. Orthonormal orbitals for the representation of an arbitrary density. *Phys. Rev. A*, **24**; pp. 680–682, 1981. 28

[65] M. Levy. Universal variational functionals of electron densities, first-order density matrices, and natural spin-orbitals and solution of the v-representability problem. *Proceedings of the National Academy of Sciences*, **76**, no. 12; pp. 6062–6065, 1979. 28

[66] G. Vignale and M. Rasolt. Density-functional theory in strong magnetic fields. *Physical Review Letters*, **59**; pp. 2360–2363, 1987. 28

[67] K. Capelle and G. Vignale. Nonuniqueness of the Potentials of Spin-Density-Functional Theory. *Phys. Rev. Lett.*, **86**; pp. 5546–5549, 2001. 28

[68] W. Kohn and L. J. Sham. Self-Consistent Equations Including Exchange and Correlation Effects. *Phys. Rev.*, **140**; pp. A1133–A1138, 1965. 28

[69] E. H. Lieb and S. Oxford. Improved lower bound on the indirect Coulomb energy. *International Journal of Quantum Chemistry*, **19**, no. 3; pp. 427–439, 1981. ISSN 1097-461X. 28

[70] G. Kin-Lic Chan and N. C. Handy. Optimized Lieb-Oxford bound for the exchange-correlation energy. *Phys. Rev. A*, **59**; pp. 3075–3077, 1999. 28

[71] J. P. Perdew, K. Burke and M. Ernzerhof. Generalized Gradient Approximation Made Simple. *Phys. Rev. Lett.*, **77**; pp. 3865–3868, 1996. 30, 69

[72] J. P. Perdew, K. Burke and M. Ernzerhof. Perdew, Burke, and Ernzerhof Reply. *Phys. Rev. Lett.*, **80**; pp. 891–891, 1998. 30

[73] Y.-S. Kim, M. Marsman, G. Kresse, F. Tran and P. Blaha. Towards efficient band structure and effective mass calculations for III-V direct band-gap semiconductors. *Phys. Rev. B*, **82**; p. 205212, 2010. 30, 70

[74] F. Aryasetiawan and O. Gunnarsson. The GW method. *Reports on Progress in Physics*, **61**, no. 3; p. 237, 1998. 30

[75] M. S. Dresselhaus. *Applications of Group Theory to the Physics of Solids*, chapter 19. Spin Orbit Interaction in Solids and Double Groups. Online, 2002. Http://stuff.mit.edu/afs/athena/course/6/6.734j/www/group-full02.pdf version 8.510J, 6.734J. 34, 53

[76] G. Dresselhaus. Spin-Orbit Coupling Effects in Zinc Blende Structures. *Phys. Rev.*, **100**; pp. 580–586, 1955. 34

[77] M. Nakahara. *Geometry, topology and physics*. IOP Publishing, 1990. ISBN 0-85274-095-6. 36

[78] Y. Hatsugai. Chern number and edge states in the integer quantum Hall effect. *Phys. Rev. Lett.*, **71**; pp. 3697–3700, 1993. 36

[79] T. Fukui and Y. Hatsugai. Quantum Spin Hall Effect in Three Dimensional Materials: Lattice Computation of Z_2 Topological Invariants and Its Application to Bi and Sb. *Journal of the Physical Society of Japan*, **76**, no. 5; p. 053702, 2007. 37, 42

[80] T. Fukui, T. Fujiwara and Y. Hatsugai. Topological Meaning of Z_2 Numbers in Time Reversal Invariant Systems. *Journal of the Physical Society of Japan*, **77**, no. 12; p. 123705, 2008. 37

[81] R. Roy. Z_2 classification of quantum spin Hall systems: An approach using time-reversal invariance. *Phys. Rev. B*, **79**; p. 195321, 2009. 37

[82] Z. Wang, X.-L. Qi and S.-C. Zhang. Equivalent topological invariants of topological insulators. *New Journal of Physics*, **12**, no. 6; p. 065007, 2010. 37

[83] R. Resta. Macroscopic polarization in crystalline dielectrics: the geometric phase approach. *Rev. Mod. Phys.*, **66**; pp. 899–915, 1994. 37

[84] L. Fu, C. L. Kane and E. J. Mele. Topological Insulators in Three Dimensions. *Phys. Rev. Lett.*, **98**; p. 106803, 2007. 41, 45

[85] R. Roy. Topological phases and the quantum spin Hall effect in three dimensions. *Phys. Rev. B*, **79**; p. 195322, 2009. 41

[86] R. Yu, X. L. Qi, A. Bernevig, Z. Fang and X. Dai. Equivalent expression of $\mathbb{Z}_2$ topological invariant for band insulators using the non-Abelian Berry connection. *Phys. Rev. B*, **84**; p. 075119, 2011. Preprint on http://arxiv.org/abs/1101.2011. 42, 43

[87] W. Feng, J. Wen, J. Zhou, D. Xiao and Y. Yao. First-principles calculation of Z_2 topological invariants within the FP-LAPW formalism. *Computer Physics Communications*, **183**, no. 9; pp. 1849–1859, 2012. Preprint online http://arxiv.org/abs/1107.2679. 42

[88] S. Murakami and S.-i. Kuga. Universal phase diagrams for the quantum spin Hall systems. *Phys. Rev. B*, **78**; p. 165313, 2008. 44

[89] S. Murakami. Gap closing and universal phase diagrams in topological insulators. *Physica E*, **43**; pp. 748–754, 2011. 44

[90] L. Winterfeld, L. A. Agapito, J. Li, N. Kioussis, P. Blaha and Y. P. Chen. Strain-induced topological insulator phase transition in HgSe. Submitted to Phys Rev B on Nov 23, 2012, accepted on Feb 15, 2013; online http://arxiv.org/abs/1302.4125. 46

[91] O. Madelung (editor). *Data in Science and Technology: Semiconductors Other Than Group IV Elements and III–V Compounds*. Springer, Berlin, 1992. 46, 47

[92] S. Radescu, A. Mujica, J. López-Solano and R. J. Needs. Theoretical study of pressure-driven phase transitions in HgSe and HgTe. *Phys. Rev. B*, **83**; p. 094107, 2011. 46, 47, 52

[93] K.-U. Gawlik, L. Kipp, M. Skibowski, N. Orłowski and R. Manzke. HgSe: Metal or Semiconductor? *Phys. Rev. Lett.*, **78**; pp. 3165–3168, 1997. 47

[94] M. von Truchsess, A. Pfeuffer-Jeschke, C. R. Becker, G. Landwehr and E. Batke. Electronic band structure of HgSe from

Fourier transform spectroscopy. *Phys. Rev. B*, **61**; pp. 1666–1669, 2000. 48

[95] A. Delin. First-principles calculations of the II-VI semiconductor β-HgS: Metal or semiconductor. *Phys. Rev. B*, **65**; p. 153205, 2002. 48

[96] C. Janowitz, N. Orlowski, R. Manzke and Z. Golacki. On the band structure of HgTe and HgSe – view from photoemission. *Journal of Alloys and Compounds*, **328**, no. 1–2; pp. 84 – 89, 2001. ISSN 0925-8388. Proceedings of the 5th International School and Symposium on Synchrotron Radiation in Natural Science. 48

[97] S. Einfeldt, F. Goschenhofer, C. R. Becker and G. Landwehr. Optical properties of HgSe. *Phys. Rev. B*, **51**; pp. 4915–4925, 1995. 48, 49

[98] A. Svane, N. E. Christensen, M. Cardona, A. N. Chantis, M. van Schilfgaarde and T. Kotani. Quasiparticle band structures of β-HgS, HgSe, and HgTe. *Phys. Rev. B*, **84**; p. 205205, 2011. 49

[99] A. Fleszar and W. Hanke. Electronic structure of II^B-VI semiconductors in the GW approximation. *Phys. Rev. B*, **71**; p. 045207, 2005. 49

[100] R. Sakuma, C. Friedrich, T. Miyake, S. Blügel and F. Aryasetiawan. GW calculations including spin-orbit coupling: Application to Hg chalcogenides. *Phys. Rev. B*, **84**; p. 085144, 2011. 49

[101] C.-Y. Moon and S.-H. Wei. Band gap of Hg chalcogenides: Symmetry-reduction-induced band-gap opening of materials with inverted band structures. *Phys. Rev. B*, **74**; p. 045205, 2006. 50

[102] A. Jayaraman, W. Klement and G. C. Kennedy. Melting and Polymorphic Transitions for Some Group II-VI Compounds at High Pressures. *Phys. Rev.*, **130**; pp. 2277–2283, 1963. 52

[103] M. I. McMahon, N. G. Wright, D. R. Allan and R. J. Nelmes. High-pressure crystal structure of HgTe-IV. *Phys. Rev. B*, **53**; pp. 2163–2166, 1996. 52

[104] K. Park, J. J. Heremans, V. W. Scarola and D. Minic. Robustness of Topologically Protected Surface States in Layering of Bi_2Te_3 Thin Films. *Phys. Rev. Lett.*, **105**; p. 186801, 2010. 62

[105] J. Vidal, X. Zhang, L. Yu, J.-W. Luo and A. Zunger. False-positive and false-negative assignments of topological insulators in density functional theory and hybrids. *Phys. Rev. B*, **84**; p. 041109, 2011. 66

[106] P. E. Blöchl. Projector augmented-wave method. *Phys. Rev. B*, **50**; pp. 17953–17979, 1994. 69

[107] H. J. Monkhorst and J. D. Pack. Special points for Brillouin-zone integrations. *Phys. Rev. B*, **13**; pp. 5188–5192, 1976. 69

[108] F. D. Murnaghan. The Compressibility of Media under Extreme Pressures. *Proceedings of the National Academy of Sciences*, **30**, no. 9; pp. 244–247, 1944. 69

[109] A. D. Becke and E. R. Johnson. A simple effective potential for exchange. *The Journal of Chemical Physics*, **124**, no. 221101, 2006. 70